university of groningen / faculty of science and engineering

# Simulating and Designing a Telecommunication System for a Martian Rover

BSc Astronomy

*Astronomy Bachelor's Thesis Project*

*Author*: Andreea Cistina Popescu
*Student nr.*: S4303458
*e-mail*: a.popescu.8@student.rug.nl

*Supervisors*:
Prof. Dr. Andrey Baryshev

6th of August 2025

# Abstract

This study presents a detailed evaluation of a dual-band communication system for a Martian rover, designed to operate with 2.4 GHz antennas for control and sensor data, and 5.8 GHz antennas for high-bandwidth video transmission. Extensive simulation-based analysis was conducted in *CST Microwave Studio* to optimize impedance matching, antenna placement, and inter-system isolation.

Several positioning strategies were explored, revealing trade-offs between gain and coverage uniformity, particularly when mounting antennas directly on the chassis versus elevated on masts. Dual-antenna configurations, implemented at both frequencies, proved effective in enhancing signal stability, mitigating nulls caused by structural interference, and preserving link integrity across various rover orientations.

System-level evaluations demonstrated that the 2.4 GHz control link offers reliable omnidirectional coverage with low power requirements. In comparison, the 5.8 GHz video link, supported by a high-gain base station antenna, provides robust communication.

# Acknowledgments

This thesis would not have been possible without the support and guidance of several individuals and teams, to whom I am deeply thankful.

First, I would like to thank the Makercie rover team from the university. Their dedication and collaboration provided me with the invaluable opportunity to engage with a hands-on engineering project, including the design and simulation of a functional rover for real-world applications.

I am also sincerely thankful to the Astronomy Bachelor's coordination team for their understanding and support during my medical challenges, which delayed the completion of my bachelor's project. Their flexibility made it possible for me to continue and complete this work.

My gratitude goes as well to Ing. Simon Busman, who introduced me to the fundamentals of communication systems and electronics. His guidance and willingness to share knowledge were instrumental in shaping my technical understanding throughout this project.

Finally, I would like to thank my thesis supervisor, Prof. Dr. Andrey Baryshev, for supporting my proposal, for contributing his expertise to the rover project, and allowing me the freedom to pursue a thesis topic aligned with my interests and the ongoing work of the rover team, also helping me design the antennas through the thesis project, and also for the very much appreciated free coffee.

Additionally, I would like to acknowledge the occasional use of AI-based tools for assistance with grammar and overcoming writing blocks during the preparation of this thesis.

# Contents

# Chapter 1: Introduction

## 1.1 Space Missions

Throughout history, exploration has been one of humanity's most ambitious endeavors, driven by the desire to expand knowledge and understanding. In recent decades, the drive to explore has extended beyond Earth, into the vastness of the universe. This pursuit has relied on a vast array of technologies, each playing a critical role in empowering missions, collecting data, and ensuring the survival and success of spacecraft and astronauts.

Most of the technology used for space exploration is kept within the solar system since it provides the only known example of habitable planets, the only star we can observe close-up, and the only worlds that can be visited with space probes [1]. Therefore, most space missions would adopt technology such as fly-bys, orbiters, landers, and rovers [2].

The apparent target for planetary exploration within the solar system is Mars. The Red Planet stands out as the top target for planetary exploration due to its proximity, scientific potential, and role as a bridge to human spacefarers [3]. As the most Earth-like planet, it allows missions to reach it within 6 to 9 months [4]. Mars once hosted liquid water, a thicker atmosphere, and habitable conditions that may have supported microbial life, making it a premier target to search for bio-signatures and understand planetary evolution [3].

## 1.2 Martian Rovers

In November 1970, the Soviet *Luna17* lander deployed *Lunokhod1*, the first remote-controlled robotic rover to operate on the Moon's surface, intended for about three months, it ultimately drove more than 10 km over 11 months and returned thousands of images [5]. Nearly 27 years later, NASA's Sojourner, aboard the Mars Pathfinder lander, rolled onto Mars on July 4, 1997, initially slated for a seven-sol mission but lasted 83 sols, ushering in persistent Martian rover operations [6]. In January 2004, NASA launched twin rovers Spirit (Gusev Crater) and Opportunity (Meridiani Planum); though nominally 90-sol missions, Spirit ultimately worked until 2010 and Opportunity until mid-2018, radically expanding our understanding of Mars' watery past [7]. Two years later, on August 6, 2012, the SUV-size rover Curiosity (Mars Science Laboratory) landed in Gale Crater to assess ancient habitability and remains active into 2025 [8].

Rovers have become essential tools in space exploration, particularly in studying planetary surfaces, like Mars. These robotic vehicles are designed to travel across the terrain of celestial bodies, collecting data, conducting experiments, and providing insights that would be difficult or impossible to obtain [9]. These machines have transformed our understanding of Mars and other worlds, playing a critical role in the search for life, studying planetary geology, and preparing for future human exploration.

The primary advantages of rovers are their mobility and the wide range of scientific instruments that enable them to conduct complex analyses on-site. Such equipment includes cameras, spectrometers, environmental sensors, drills, and even miniature laboratories capable of identifying organic molecules and studying the chemical composition of soil and rocks. By performing science directly on the surface, rovers reduce the need to bring large quantities of material back to Earth, which is currently expensive and technically challenging [11].

## 1.3 Communication Systems of Rovers

At the heart of these robotic missions lies the wireless communication system, which has become a cornerstone of modern space exploration and plays a particularly vital role in operating planetary rovers. These robotic explorers rely entirely on wireless systems to transmit data, receive commands, and maintain operational coordination with orbiters and ground stations on Earth [12]. Without reliable wireless communication, rovers could not conduct scientific investigations, navigate terrains,

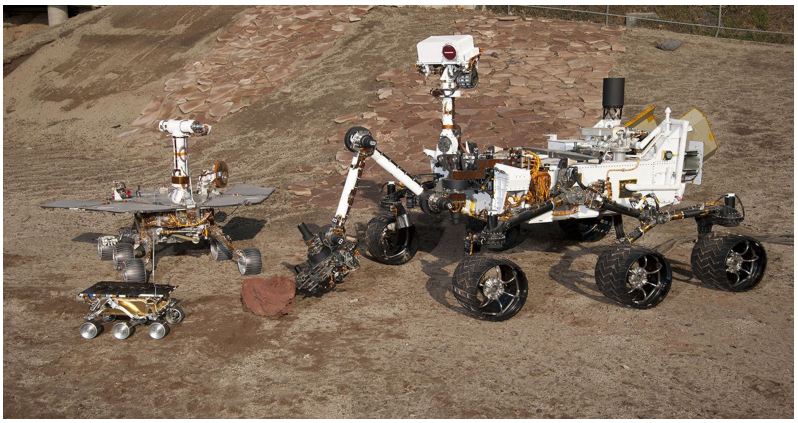

*Figure 1.1: Three Generations of Rovers at NASA's Jet Propulsion Laboratory's Mars Yard. Image by NASA's Jet Propulsion Laboratory [10]*

or return valuable information to mission control. In this context, wireless technology is not just a convenience; it has become the essential link that enables remote, autonomous exploration of outer worlds.

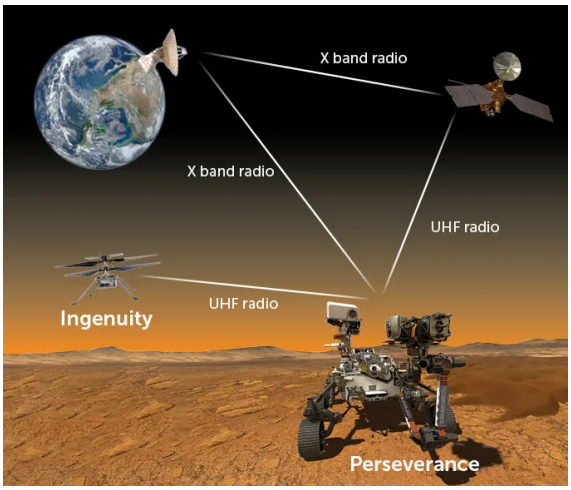


*Figure 1.2: Perseverance's communication system with Inginuity via UHF Radio, Earth via X-band and UHF Radio to Mars Reconnaissance Orbiter. Image adapted by C. Chang. Elements from NASA, JPL-Caltech/NASA, and Anita Gould (Flickr, CC BY-NC 2.0)[13]*

The most fundamental function of wireless communication in rover missions is the transmission of data. Rovers are equipped with numerous instruments that generate large volumes of scientific data. This information must be transmitted wirelessly either directly to Earth or, more commonly, to an orbiting relay satellite, which beams the data back to mission control on Earth.

Since rovers are highly restricted in mass, power, and antenna size, direct-to-Earth links would be slow. By contrast, a surface-based station can house significantly larger antennas and more powerful transmitters, enabling much higher throughput. This allows rovers to be lighter and simpler, optimizing their design for science operations rather than communication systems.

In addition to sending data, wireless communication is essential for receiving commands from Earth. Since rovers operate at vast distances of up to 400 million kilometers away, direct real-time control is impossible due to signal delay. Instead, this paper will focus on a simpler design for the relay station(where data transmission will be directed toward a Martian station) rather than

Earth or the orbiting relay satellite. These commands can include navigation routes, operational sequences for scientific experiments, or system updates. The reliability of wireless links ensures that commands are received accurately, allowing the rover to perform tasks safely and efficiently.

## 1.4 European Rover Challenge(ERC)

This thesis is written in collaboration with the Rijksuniversiteit Groningen team (Makercie) for the ERC competition, one of the world's premier international robotics competitions, geared explicitly towards planetary exploration. Held annually in Poland, the ERC brings together university teams from around the globe to design, build, and operate Mars rover prototypes in simulated Martian environments. The event is inspired by the real-world challenges faced by robotic missions on Mars, such as navigating difficult terrain, collecting geological samples, and performing autonomous maintenance tasks.

*Figure 1.3: Photo of the Makercie team*

The competition demands that each team have a wireless communication system for each rover; therefore, due to differences in terrain, distance, and the inability to see the rover at all times, the report will primarily focus on applying the theoretical background of antenna geometry theory to design, simulate, and test the robustness and efficiency of the two transmission and receiving systems that the rover will utilize during the competition.

# Chapter 2: Theory

## 2.1 Principles

This section outlines the fundamental concepts underlying antenna design. The discussion focuses on the necessary physical and electrical conditions for radiation and examines the spatial regions associated with antenna fields. Understanding these principles is crucial for analyzing antenna behavior and designing systems that facilitate efficient energy transfer.

### 2.1.1 Definition of an Antenna

At a fundamental level, an antenna is a device that converts guided waves present in a waveguide, feeder cable, or transmission line into radiating waves traveling in free space, or vice versa. In principle, if the voltage source is sinusoidal, the electric field will also vary sinusoidally at the same frequency. These time-varying electric and magnetic fields propagate as electromagnetic waves along the transmission line toward the antenna, as observed in *Figure 2.1.* As the waves enter the antenna, they are associated with charges and currents on its structure. If part of the antenna is removed, as shown in *Figure 2.1b*, the open ends of the E-field lines, represented by dashed lines, connect to free space, thereby forming radiated waves. These free-space waves remain periodic, and a point of constant phase $P_0$ moves outward at the speed of light, traversing $\lambda/2$ to reach $P_1$ in half a period [14].

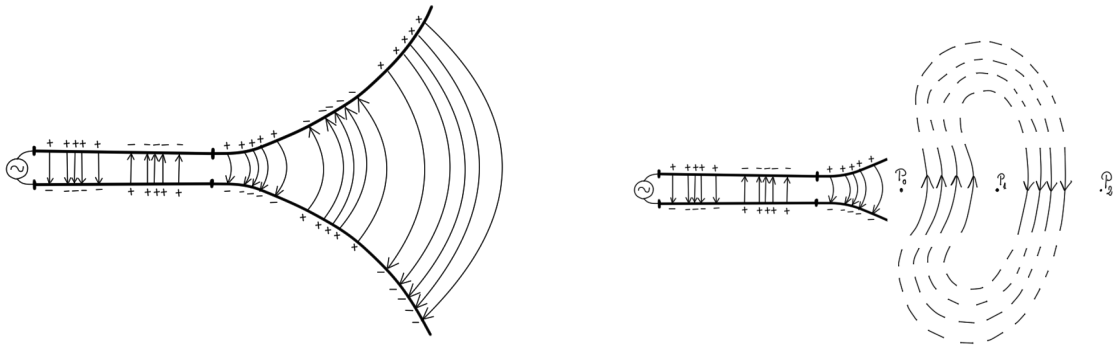

(a) Antenna and the electric field lines

(b) Antenna and the free-space wave

*Figure 2.1: Source, transmission line, antenna, and detachment of electric field lines*

## 2.2 Antenna Parameters

Efficient radiation requires the antenna to be resonant at the operating frequency. This typically means the antenna's physical dimensions should be a specific fraction of the wavelength. Resonance minimizes the antenna's reactance, allowing maximum power transfer and efficient radiation [14].

### 2.2.1 Radiation Pattern

An antenna's radiation pattern graphically represents its far-field radiated energy as a function of direction, defined in space coordinates. It illustrates how power flux density, radiation intensity, field strength, directivity, phase, and polarization vary with the observer's angular coordinates. In mathematical terms, the pattern is the spatial distribution of radiated energy on a spherical surface of constant radius, parameterized by the observer's angles in a spherical coordinate system, as seen in *Figure 2.2.* This relationship between Cartesian and spherical coordinates allows one to translate physical directions into angular variables for plotting and analysis [15].

Both field and power patterns are typically normalized to their respective maxima and plotted on a logarithmic(decibel) scale. Using decibels makes low-level features of the pattern more visible,

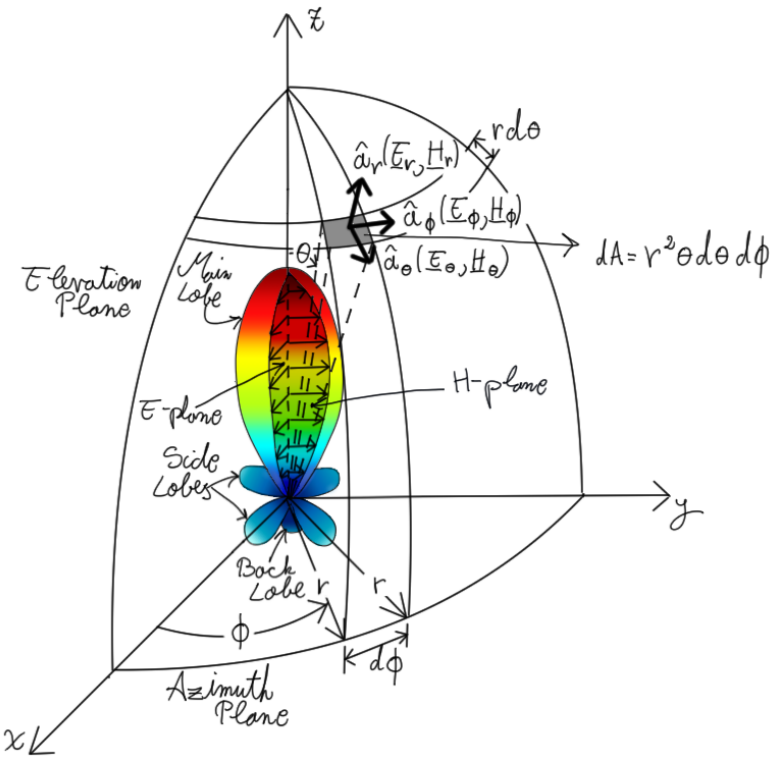


*Figure 2.2: Coordinate system for antenna analysis in Cartesian and spherical coordinates*

highlighting details in regions of very low intensity that would otherwise be difficult to observe. This normalization also facilitates direct comparison between antennas or configurations by removing absolute amplitude differences and focusing on relative variations [14].

A radiation lobe is defined as a region of the pattern bounded by areas of relatively low intensity. In a symmetric three-dimensional polar representation, as observed in *Figure 2.2*, several lobes may appear: the main lobe, which has the highest intensity; side lobes, which are smaller lobes outside the main beam; and back lobes, which lie approximately opposite the main lobe. Specifically, the main beam contains the direction of maximum radiation(at $\theta = 0$) while side lobes represent radiation in unintended directions. A back lobe, by definition, is a lobe whose axis is approximately $\theta = 180^\circ$ from the main beam [15].

Side lobes are generally undesirable in directional antennas because they represent wasted radiation in unintended directions. The side-lobe level is quantified as the power density ratio in a given side lobe to that of the main lobe. For most directional antennas, side-lobe levels below $-20dB$ are preferred to ensure efficient radiation and minimal interference [15].

Radiation patterns are often classified into three broad categories. The isotropic pattern is a theoretical reference: it corresponds to a hypothetical lossless antenna that radiates equally in all directions. In the case for an omnidirectional pattern, this is a special case of a directional pattern that is uniform in one plane(the azimuthal plane $f(\phi)$ at $\theta = \pi/2$) and directional in the orthogonal plane (the elevation plane $g(\theta)$ at $\phi =$ constant). In this sense, an omnidirectional antenna radiates equally around a horizontal circle but varies with elevation, as illustrated in *Figure 2.3* [15].

In contrast, a directional pattern concentrates radiation more effectively in specific directions than in others, typically exhibiting directivity greater than that of a half-wave dipole; examples of such antennas are illustrated in *Figures 2.2.*

For linearly polarized antennas, performance is further described by principal electric(E-) and

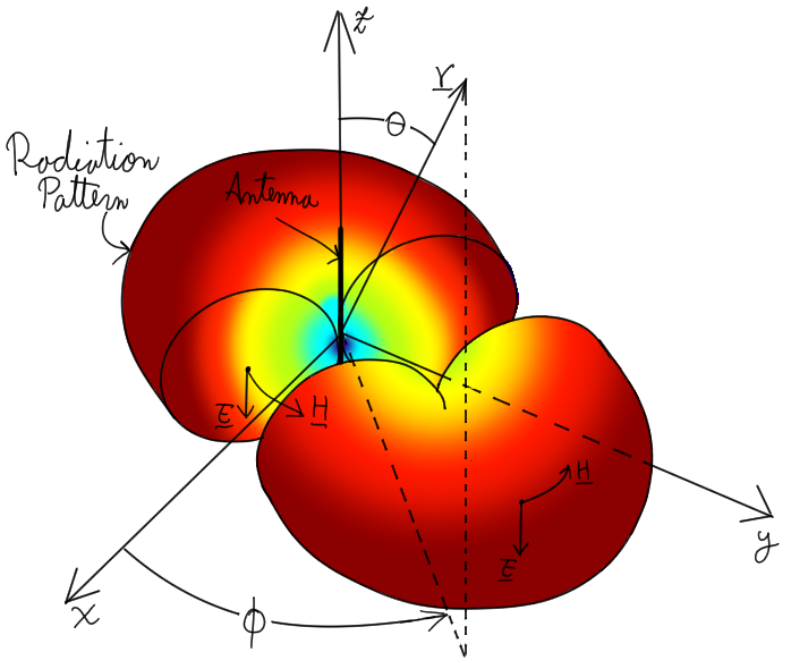


*Figure 2.3: Omnidirectional antenna pattern.*

magnetic(H-) plane patterns. The E-plane contains the E-field vector and the direction of maximum radiation, while the H-plane contains the H-field vector and the same principal direction. These planes are illustrated in *Figure 2.2* and are essential for understanding how polarization affects an antenna's radiation characteristics [15].

As the observation distance transitions from the reactive near-field to the far-field region, an antenna's amplitude pattern changes due to variations in the magnitude and phase of the electromagnetic fields. *Figure 2.2* illustrates a typical evolution of the radiation pattern for an antenna with a maximum dimension[15].

### 2.2.2 Field Regions

Close to an antenna, the field patterns change rapidly with distance, including radiating and reactive energy. This space found around the antenna can be divided into three regions: reactive near field, radiating near-field (Fresnel), and far-field(Fraunhofer) regions, as seen in *Figure 2.4*.

**Reactive-near filed region**

This region immediately surrounds an antenna, where reactive non-radiating fields dominate. For most antenna types, the outer limit of this region is typically defined by the condition[15]:

$$R_1 < 0.62\sqrt{\frac{D^3}{\lambda}} \tag{2.1}$$

Where:

- $D$ is the antenna's maximum dimension;
- $\lambda$ is the associated wavelength.

**Radiating near-field (Fresnel) region**

The Fresnel region lies between an antenna's reactive near-field and far-field zones. In this region, radiating fields dominate; however, the angular distribution of the fields varies with distance from

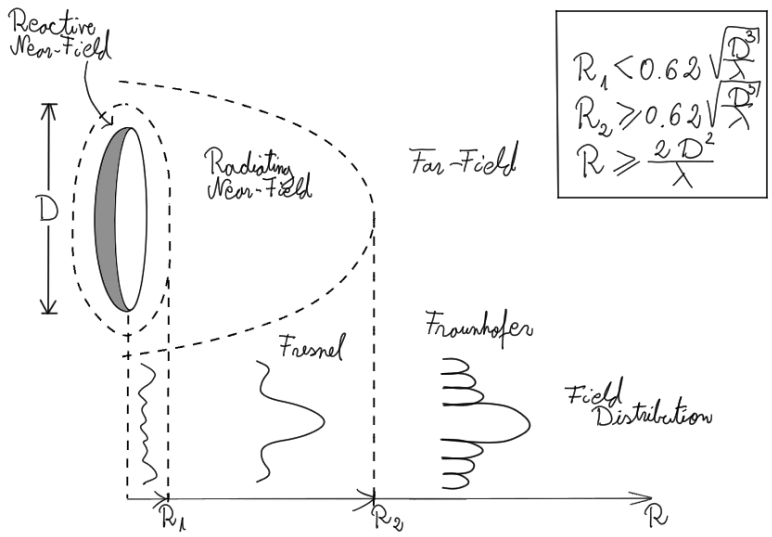


*Figure 2.4: Field region and changes of amplitude pattern from reactive near-field towards far-field for an antenna*

the antenna. This region may not be present if the antenna's maximum dimension is small relative to the wavelength.

The inner boundary of the radiating near-field is typically defined as:

$$R_2 \geq 0.62\sqrt{\frac{D^3}{\lambda}} \tag{2.2}$$

These bounds are based on a maximum allowable phase error of $\pi/8$. Within this region, the field pattern generally depends on radial distance, and the radial component of the field can be significant [15].

**Far-field (Fraunhofer) region**
The Fraunhofer region is the area around an antenna where the angular distribution of the radiated field becomes effectively independent of distance from the antenna. For an antenna with a maximum overall dimension $D$, this region is generally considered to begin at:

$$R \geq \frac{2D^2}{\lambda} \tag{2.3}$$

The radiated field components in this region are predominantly transverse, and the radiation pattern does not change with radial distance [15].

### 2.2.3 The Scattering Parameter Matrix

The scattering parameter matrix (or S-parameter matrix) describes how electromagnetic waves behave at the ports of a networked system, such as an antenna, filter, or amplifier, by relating incident and reflected signal components in the frequency domain [16].

For antenna design, the most important element of the matrix is the S11 parameter, since it indicates how much power is reflected due to impedance mismatch. A well-tuned antenna exhibits a $|S11| < -10$ dB, meaning that over 90% of the radiation is of the input power is radiated or absorbed, and less than 10% is reflected. The frequency at which the S-parameter drops under -10dB shows at which frequency the system resonates, and the bandwidth is determined by the frequency range over which |S11| stays under this threshold [16].

### 2.2.4 Bandwidth

The bandwidth of an antenna is defined as the range of frequencies over which it can operate effectively.

Using Shannon's limit, the theoretically required bandwidth B[Hz] formula is [17]:

$$B = C \left[ \log_2 \left( 1 + \frac{S}{N} \right) \right]^{-1} \tag{2.4}$$

Where:

- C is the channel capacity [$\mathrm{bit\,s^{-1}}$]
- $\frac{S}{N}$ is the signal to noise power ratio $\approx 100$[17]

The $\frac{S}{N}$ was approximated to be 100 in order to assume that the system delivers robust performance with low error rates [18].

To determine the ideal operating frequency of an antenna for a system, the bandwidth-to-frequency ratio must be significantly smaller than 1. Therefore, assuming that the center frequency is $B$, this gives:

$$F_B = \frac{B}{f} \ll 1 \tag{2.5}$$

### 2.2.5 Transmission Power

In a non-idealistic system, it is necessary to calculate the impact of noise on the system, since $\frac{S}{N}$ will determine the system's performance.

In the transmitting-antenna circuit shown in *Figure 2.5*, the input resistance is divided into two components: radiation resistance ($R_r$), which corresponds to the power radiated by the antenna, and loss resistance ($R_l$), which accounts for unwanted power dissipation, this usually releases in the conductive and dielectric material of the antenna system [14].

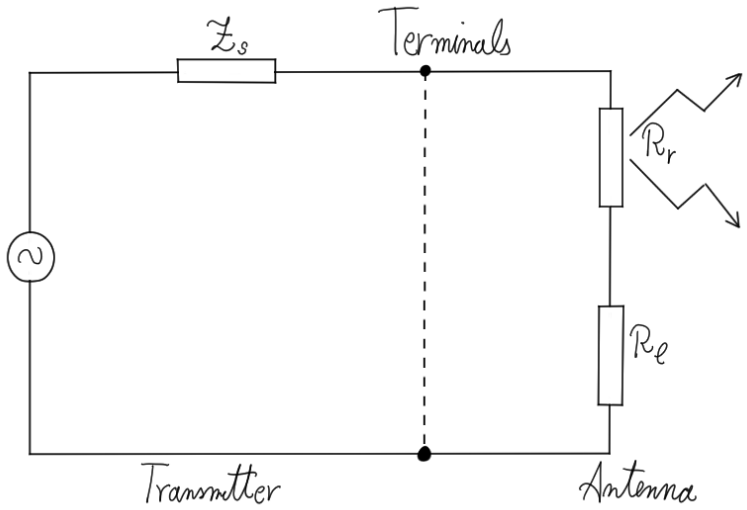


*Figure 2.5: Simple circuit of transmitting antenna*

The noise power $P_r$[W] delivered to the input of a network by a resistor at a given absolute temperature is:

$$P_r = kTB \tag{2.6}$$

Where:

- k is the Boltzmann constant $\approx 1.381 \times 10^{-23} W\, Hz^{-1}\, K^{-1}$ [19];
- T is the temperature noise;
- B is the communication bandwidth [Hz]

The temperature noise can be calculated from:

$$T = 290K(10^{\frac{NF}{10}} - 1) \tag{2.7}$$

Where $NF$ is the noise figure, and assuming a robust communication system, the noise figure can be approximated to $NF = 1$ dB ($\approx 1.26$ in linear scale)[20]. So an idealized system will have a noise temperature of approximately 75 K.

For communication between two antennas separated by a distance of $R > \frac{2D^2}{\lambda}$(the Far-Field region), the power transmitted for reflection and polarization-matched antennas aligned for maximum direction radiation and reception would follow the *Friis Transmission Equation*[15]:

$$\frac{P_r}{P_t} = G_r G_t \left(\frac{\lambda}{4\pi R}\right)^2 \tag{2.8}$$

Where:

- $P_r$ is the received power
- $P_t$ is the required transmitted power
- $G_r$ is the receiving antenna gain
- $G_t$ is the transmitted antenna gain
- $R$ is the maximum path length

Where the linear gain can be calculated from the linear directivity $D(\theta, \phi)$ and the efficiency of an apparatus by[15]:

$$G(\theta, \phi) = \eta\, D(\theta, \phi) \tag{2.9}$$

## 2.3 Dipole Antenna

When a two-wire transmission line is driven by a source at one end and left open at the other, the incident wave reflects at the open end. It travels back, combining with the forward wave to create a standing-wave pattern of current with nodes half a wavelength apart and a current of zero at the open termination. Because the currents in the two conductors flow in opposite directions, their radiated fields cancel each other out. No energy is emitted into the far field. However, if the final half-wavelength of the line is bent outward to form a straight element perpendicular to the original conductors, see *Figure 2.6*, the currents on that bent segment flow parallel and in phase, producing radiation and thus converting that section into a dipole [14].

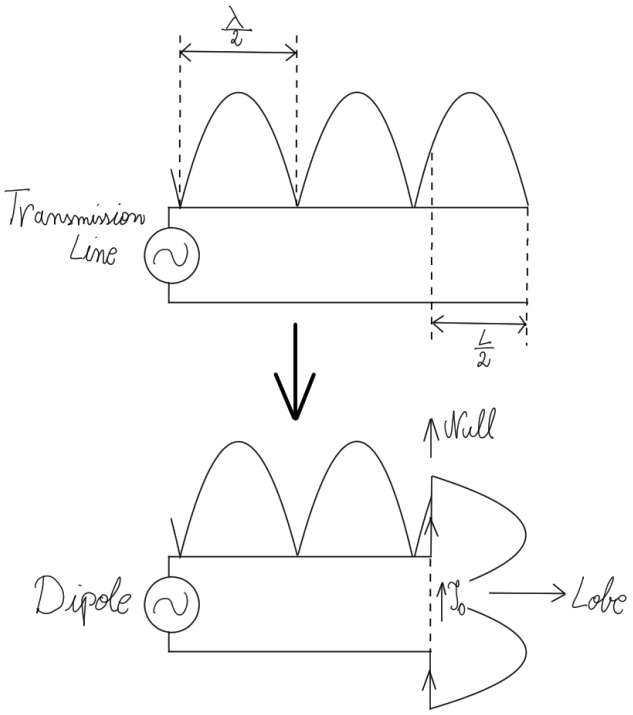


*Figure 2.6: The transformation from a simple transmission line to a dipole antenna*

### 2.3.1 Half Wavelength Dipole

The resonant length $L$ of a center-fed half-wave dipole antenna is determined by its associated wavelength. At resonance, the total length of the dipole corresponds approximately to half the wavelength:

$$L = \frac{\lambda}{2} \tag{2.10}$$

This length ensures that the antenna supports a standing wave with a current maximum at the center and voltage maxima at the ends, maximizing radiation efficiency in the broadside direction [14].

The physical radius $r$ of the dipole plays a significant role in determining the antenna's bandwidth and input impedance. To maintain desirable radiation characteristics and ensure the thin-wire approximation remains valid, the condition typically constrains the dipole radius:

$$r \leq \frac{\lambda}{20} \tag{2.11}$$

While this expression defines the upper limit, any smaller radius may also be used, provided it satisfies mechanical and fabrication constraints[15].

### 2.3.2 Quarter-Monopole Antennas

The quarter-wave monopole antenna is conceptually derived from the half-wave dipole by exploiting the method of image theory. Instead of employing two conductive arms, a single vertical conductor is positioned above a Perfect Electric Conductor(PEC) plane, which acts as a mirror image of the missing lower half, as seen in *Figure 2.9*.

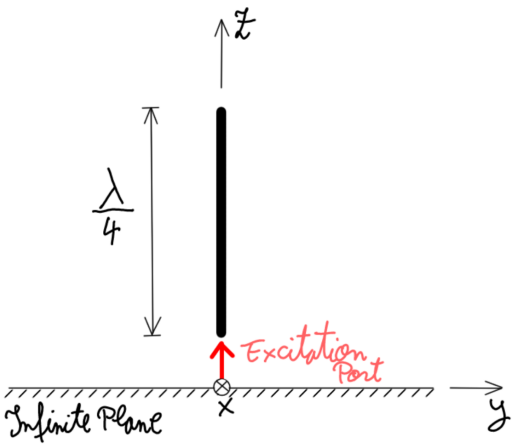


*Figure 2.7: Simple representation of the quarter-wave monopole over an infinite plane*

Due to the symmetry imposed by the PEC ground plane, the physical length $L$ of a quarter-wave monopole is half that of a resonant dipole:

$$L = \frac{\lambda}{4} \tag{2.12}$$

This length supports a standing wave with a current maximum at the base and a null at the free end, radiating predominantly in the hemisphere above the ground plane [15].

The performance of a monopole antenna is strongly dependent on the electrical size and configuration of the ground plane. In practical implementations, a ground plane sizes below $0.25\lambda$ significantly impact resonant frequency and matching, while above this threshold, effects diminish; therefore, the lower bound of the ground plane can be approximated to [21]:

$$g \geq \frac{\lambda}{4} \tag{2.13}$$

## 2.4 Directional Antenna

Unlike omnidirectional antennas, which radiate uniformly in the azimuthal plane, directional antennas concentrate electromagnetic energy into a specific direction. This focused radiation improves gain, enhances range, and reduces susceptibility to interference from unwanted directions.

### 2.4.1 Plane Reflector

The simplest type of reflector is a plane reflector. Such an arrangement is shown in *Figure 2.8* and can be easily constructed using a PEC plane together with an omnidirectional feed point, such as a dipole antenna. The addition of a reflector effectively transforms an omnidirectional feed into a directional antenna, with improved gain in the desired direction.

When a radiating element is placed in front of a sufficiently large PEC surface, the conductor reflects incident electromagnetic waves. These reflected waves combine with the directly radiated waves, and depending on the relative phase, they can interfere constructively in the forward direction(broadside) and destructively in the backward direction. This interference pattern results in increased gain, an improved front-to-back ratio, and a narrower radiation beam.

For constructive interference to occur in the forward direction, the feed must be positioned at a specific distance $h$ from the reflector. Based on path equivalence and phase symmetry, the half-wavelength criterion for the image dipole distance:

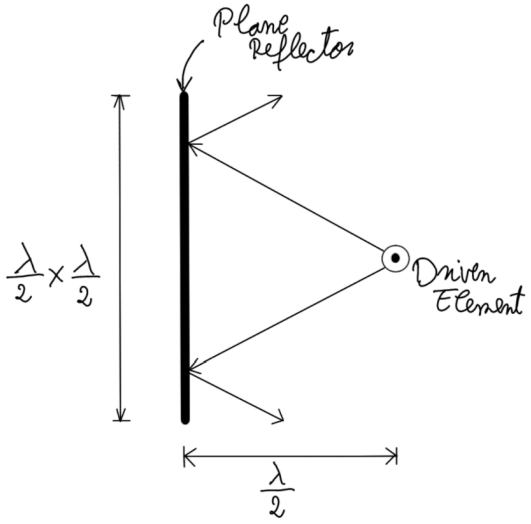


*Figure 2.8: Plane reflector antenna schematic*

$$h = \frac{\lambda}{2} \tag{2.14}$$

### 2.4.2 Parabolic Reflector Antennas

The most widely used directional antenna configuration is the parabolic reflector antenna, shown schematically in Figure 2.9. This design consists of a radiating feed element positioned at the focal point of a parabolic surface, which reflects incident spherical wavefronts into collimated plane waves. The result is a highly directional, high-gain beam with minimal divergence.

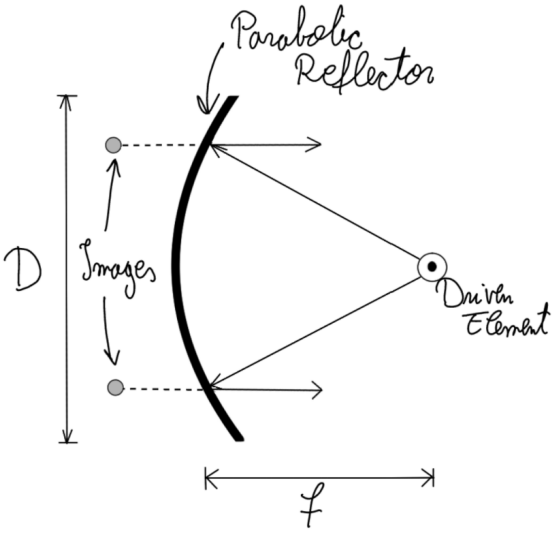


*Figure 2.9: 2D representation of a parabolic reflector*

Proper placement of the driven element at the geometric focus of the paraboloid is critical to achieving optimal performance. At this position, waves emitted by the feed are reflected such that they remain in phase across the aperture, producing a coherent and collimated main lobe. Any deviation from this focal point introduces phase errors, resulting in beam distortion, reduced

forward gain, increased sidelobe levels, and spillover losses, ultimately degrading aperture efficiency [14].

For a parabolic reflector, to find a suitable focal distance, this is calculated by approximating that the focal-to-diameter ratio($f/D$) is around 0.4.

Another critical characteristic of directional antennas is the beamwidth, which quantifies the angular extent of the main radiation lobe. Specifically, the Half-Power Beamwidth (HPBW) is defined as the angular separation between the points on the main lobe where the radiated power drops to half(-3 dB) of its peak value. The HPBW provides a practical measure of the antenna's angular resolution and is inversely related to directivity [15].

An approximate expression for the HPBW of a parabolic reflector, expressed in degrees, is given by [15]:

$$\text{HPBW} \approx 2 \arctan\left(\frac{W}{2D}\right) \tag{2.15}$$

Where:

- $W$ is the maximum width;
- $D$ is the maximum distance;

### 2.4.3 Off-center Feed Reflector Structure

A key variation of the standard parabolic reflector antenna is the off-center feed configuration. In this arrangement, the feed element is deliberately displaced laterally from the central axis of the dish. The reflector itself is no longer a full symmetrical paraboloid but rather a segmented portion of the surface, such that the focal point is relocated away from the physical center of the reflector aperture.

This architectural design, illustrated in Figure 2.10, can be described as a section of a parent paraboloid whose axis is tilted relative to the optical axis of the system. The focal point of the reflector remains fixed according to geometric principles, but the dish is physically "cut" from an off-axis region of the paraboloid. The result is an eccentric or offset geometry, with the driven element located asymmetrically to one side of the aperture.

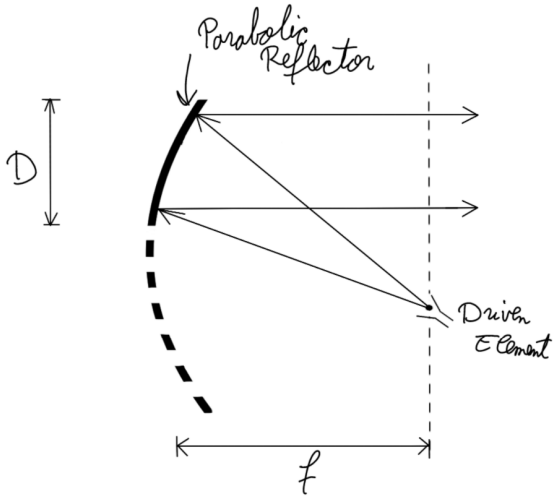


*Figure 2.10: Off-center (offset-fed) parabolic reflector configuration.*

The primary advantage of this configuration is the elimination of feed blockage. In conventional center-fed reflector systems, the feed structure and its mechanical supports are located directly

in front of the aperture, where they obstruct a portion of the radiated or received signal. This shadowing effect reduces both gain and aperture efficiency and introduces diffraction-related distortions into the radiation pattern.

By moving the feed off-axis, the main beam remains unobstructed, allowing for improved aperture efficiency due to the full utilization of the radiating surface, increased gain from reduced scattering and absorption, and a more uniform radiation pattern, as secondary lobes caused by blockage are suppressed.

Designing an off-center feed antenna involves trade-offs between structural complexity and performance benefits. The offset geometry introduces asymmetry into the system, which must be carefully compensated in the shaping of the reflector and positioning of the feed to maintain phase coherence across the aperture.

# Chapter 3: System Overview and Communication Requirements

On Mars, rover communication typically involves direct links to Earth or relay via orbiting satellites. In this thesis, it is assumed that the rover establishes direct communication exclusively with a ground station located on the same surface. This simplification serves as a foundational premise for modeling the communication system.

However, to facilitate a more controlled and computationally manageable simulation environment, the terrain is idealized as a flat plane with minor surface deformations. Within this setting, the communication system is positioned at one corner of the defined area, allowing the rover to traverse the surrounding terrain while maintaining a direct line-of-sight connection with the station.

## 3.1 Functional Architecture of the Rover-Base Communication System

On the rover, all sensor and switch data(coming from different sub-systems) are connected via CAN bus to a microcontroller that packages them over an(NRF24L01) transceiver. A matching radio at the ground station passes the packets through another microcontroller, which decodes them for display on a status/graphics panel. Meanwhile, four cameras feed a video-relay encoder, whose output is then sent via a power switch and attenuator.

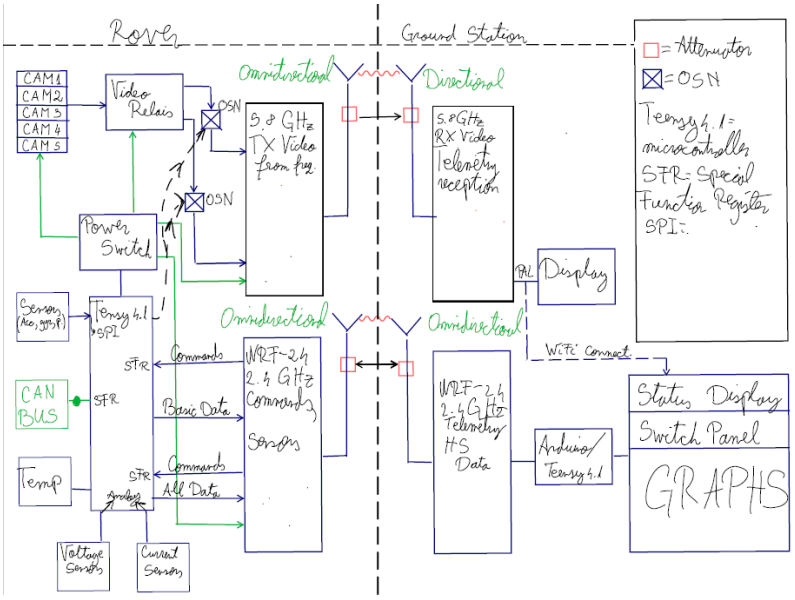


*Figure 3.1: Rover's communication system reference design*

## 3.2 Performance Requirements and Constraints

For range and data rate, the control link must support reliable bidirectional telemetry and command payloads up to 50 $m$, with a total data rate of 30 $kbps$ and latency under 50 $ms$, sufficient for real-time remote operation. While the video link must sustain 5 $Mbps$ uplink to stream 720$p$ video, with latency under 200$ms$. These measurements were chosen and calculated based on the number of sensors and data transmitted(*Appendix 8.4*). Therefore, the control latency requires strict link availability of over 99% to avoid losing rover maneuverability. While the video should tolerate

occasional frame drop, it should nonetheless maintain 95% packet delivery within a 1-minute window.

Another critical factor that affects transmission is environmental factors. Deep nulls are introduced at low-angle incidence over rocky terrain, so an omnidirectional system helps to average out fades on the control link. In this project, the elevation angle will not vary significantly, so the azimuthal angle $\theta$ will have a wide range of values. This allows the directional antenna to remain stationary at the base station without the need for a complementary system to track the signal strength of the rover at all times. In contrast, the elevation angle $\phi$ will be kept to a minimum, as the hills would not have high elevations.

The simplified(low-polygon) model of the rover inherently introduces geometric obstructions that may lead to partial or complete shadowing of the control antenna, thereby impairing signal transmission and reception. To mitigate such effects, several strategies can be employed to optimise antenna placement and maintain robust communication.

One approach involves strategically positioning the antenna at locations on the rover where structural elements are least likely to obstruct the line of sight between the antenna and the receiving station. An alternative method entails the use of a dual-antenna configuration operating at the same frequency and amplitude. By deploying two antennas simultaneously, the likelihood of both being simultaneously shadowed by the rover's structure is reduced, thereby enhancing communication reliability.

## 3.3 Selected Frequency Bands and Link Roles

Taking into account the performance requirements and system constraints outlined in Section *3.2 Performance Requirements and Constraints*, the communication architecture for the rover must include two distinct channels to ensure a complementary and reliable communication strategy. Based on the channel capacity values presented in the section mentioned above and applying *Equation 2.4*, the required bandwidths for each channel have been calculated and placed in *Table 3.1.*

To meet these bandwidth demands, two frequency bands have been selected. The first channel operates at 2.4 GHz omnidirectionally to provide a robust, low-latency control path with simple alignment requirements. The second channel operates at 5.8 GHz, providing an omnidirectional-at-rover/directional-at-base channel to deliver the high throughput needed for video without compromising the rover's agility.

| Channel no. | C[bit $s^{-1}$] | B[kHz] | $f$[GHz] | $F_B$ | $P_r$[W] |
|---|---|---|---|---|---|
| 1 | $30 \times 10^3$ | 4.51 | 2.4 | $1.88 \times 10^{-6}$ | $1.86 \times 10^{-17}$ |
| 2 | $5 \times 10^6$ | 750.95 | 5.8 | $1.29 \times 10^{-4}$ | $3.11 \times 10^{-15}$ |

*Table 3.1: Calculated bandwidth with the frequency parameters and the noise power for the channels*

As shown in Table 3.1, the calculated bandwidth fractions $F_B$ for both channels are consistent with the theoretical framework established in section *1 Bandwidth.* The selected frequencies provide sufficient bandwidth to meet the channel capacity requirements, thereby validating the suitability of the chosen frequency bands for the intended communication tasks.

### 3.3.1 Control Link at 2.4GHz, Omnidirectional-Omnidirectional

The 2.4GHz frequency was chosen for its favorable balance between antenna size, propagation characteristics, and global regulatory availability. By employing identical omnidirectional-omnidirectional antenna configurations, the system guarantees full 360° azimuth coverage and minimal pointing complexity, ensuring that command and telemetry packets are reliably exchanged even as the rover changes orientation or encounters multipath fading over mountainous terrain.

On both the rover and the ground station, omnidirectional antennas are used. This link's redundancy is critical, since if the video channel experiences a deep fade or interference, the control link remains unaffected and preserves essential rover operability.

### 3.3.2 Control Link at 5.8GHz, Omnidirectional-Directional

The video link is assigned to the 5.8 GHz band to leverage its wider available bandwidth and higher data throughput for streaming live at 720p video.

On the rover, an omnidirectional quarter monopole antenna maintains a consistent uplink pattern regardless of the vehicle's direction, simplifying onboard hardware.

At the base station, a high-gain directional reflector antenna focuses energy toward the rover's position, maximizing link margin and improving signal-to-noise ratio. This frequency separation (5.8 GHz for video, 2.4 GHz for control) also helps isolate high-bandwidth payload traffic from critical command data, reducing the risk of mutual interference.

The geometry of the directional antenna has to be carefully chosen, since it is not expected for the rover to go higher than an elevation of 2 m, and it needs to explore an area of $50 \times 50$ m, the radiation field in the elevation and azimuthal angles can be be calculated from the HPBW *Equation 2.15*.

| Plane | W[m] | D[m] | HPBW |
|---|---|---|---|
| $\theta$ | 2 | 50 | 170.85° |
| $\phi$ | 50 | 50 | 53.13° |

*Table 3.2: Values of the HPBW for the elevation and azimuthal angles*

The values for the HPBW in *Table 3* indicate the antenna concentrates energy in a fan-beam pattern.

## 3.4 Justification for Simulation-Only Approach

Adopting a simulation-only methodology for this thesis offers substantial advantages in terms of cost, schedule, and flexibility. Full-wave electromagnetic solvers enable a detailed analysis of antenna performance, including return loss, radiation patterns, gain, and efficiency, without the need for multiple hardware prototypes. Prototyping antennas at both 2.4 and 5.8 GHz, mounting them on a rover model, and testing over realistic terrain would require extensive time or access to varied field sites, driving up budget and time. In contrast, simulation allows rapid iteration on geometry, material properties, and placement parameters, accelerating the design cycle.

Simulation also provides precise control over environmental variables that are difficult to reproduce consistently in the field. By integrating a realistic desert-terrain model with soil dielectric permittivity, surface irregularities, and ground reflections into the EM solver, it is possible to systematically study diffraction, scattering, and multipath effects across a range of rover positions. Similarly, embedding a low-poly CAD representation of the rover, including metallic chassis components and supports, captures mutual coupling and structural shadowing on antenna radiation patterns. This level of parametric control ensures that performance is characterized under worst-case and nominal conditions, yielding comprehensive link-budget insights.

# Chapter 4: Simulation Setup and Methodology

## 4.1 Simulation Platform and Solvers

This thesis performs all antenna simulations using CST Studio Suite Learning Edition 2025, a leading full-wave electromagnetic simulation platform renowned for its comprehensive and high-performance capabilities [22].

At the heart of CST Studio Suite lies its electromagnetic simulation platform, Microwave Studio. The hybrid multi-solver architecture integrates time-domain, frequency-domain, integral-equation, and asymptotic solvers within a single, unified interface [23]. This flexible framework allows users to select the solver best suited to their specific application, whether broadband antenna analysis, resonant filter design, large-scale scattering studies, or multi-port interconnect modeling, without resorting to lumped-element or empirical approximations [24].

To evaluate the electromagnetic performance of the primary antennas in free space, simulations were conducted using Microwave Studio's frequency-domain and integral-equation solvers.

The frequency-domain solver is based on the finite element method (FEM), which utilizes a volumetric mesh to discretize the simulation domain. This approach is well-suited for narrow-band applications and offers high accuracy in capturing the electromagnetic behavior of complex geometries [25].

Effective mesh management balances the accuracy, convergence, and runtime of simulations to further reduce computational efforts. Adaptive tetrahedral mesh refinement is applied to the antenna structures, allowing the software to iteratively refine the mesh based on local error estimates in the electromagnetic fields. This ensures an acceptable resolution around feed points, sharp edges, and material interfaces, without unnecessarily increasing the global mesh density.

However, when simulating across a broad frequency range or in cases involving electrically large structures, the computational cost of the FEM approach increases significantly. The volumetric discretisation leads to a substantial memory footprint and extended computation time, often exceeding the capacity of standard computers. Under such constraints, the integral-equation solver provides a more efficient alternative. Unlike volumetric methods, it employs surface meshes and solves the electromagnetic problem using boundary integral formulations. This reduces memory consumption and computational complexity, particularly for open-region issues such as antenna radiation in free space [25].

Following the initial evaluation of the antenna systems in free space, the next phase involves simulating their performance in the presence of both the Martian ground surface and the rover structure. Given the electrically large dimensions of these combined elements, traditional frequency-domain or integral-equation solvers become computationally demanding due to excessive memory requirements and simulation times.

To address these challenges, the asymptotic solver is employed. This solver operates in the frequency domain and implements the Shooting and Bouncing Rays(SBR) method, a ray-tracing technique suited for high-frequency analysis involving large and complex geometries. It is particularly effective for antenna placement studies where full-wave methods are impractical [25].

In this context, the far-field radiation patterns previously computed for the antennas in free space are imported as excitation sources. These serve as input for the asymptotic solver, which then performs the electromagnetic analysis of the entire system, including interactions with the terrain and the rover body. This approach enables accurate assessment of antenna behaviour in a realistic deployment scenario while maintaining computational efficiency.

This report graphs the data of the simulations conducted using the Jupyter Notebook with Kernel Python 3(ipykernel) [26].

## 4.2 Rover and Relay Station Model Integration

The simplified rover and relay station model shown in *Figure 4.1 Figure 4.2* was designed using *SolidWorks Student Premium 2025* [22].

The rover's overall dimensions were set to approximately $200 \times 150$ cm. The model was intentionally simplified to reduce geometric complexity while preserving the structural elements critical for electromagnetic interaction analysis.

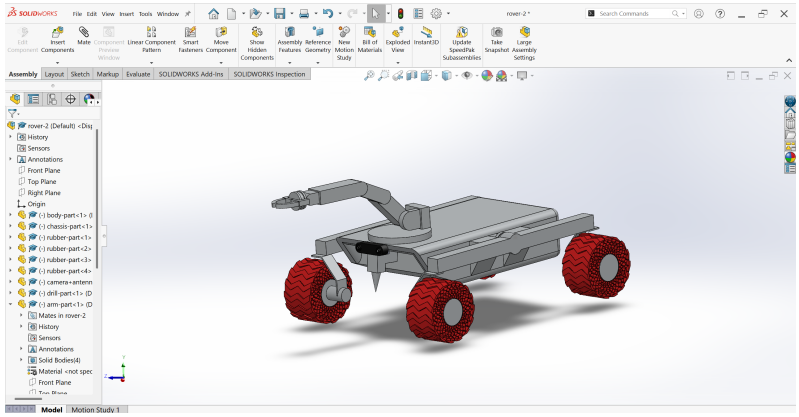

*Figure 4.1: Simplified rover geometry, without antennas*

The relay station height is around 3 m, with the direction antenna found at 1.5 m, and the omnidirectional antenna at 3 m. The placement of the antennas were planned like this since the directional antenna should not be place too high since it needs high azimuthal low elevation coverage, as it can judged from the HPBW calculations in *Table 3*.

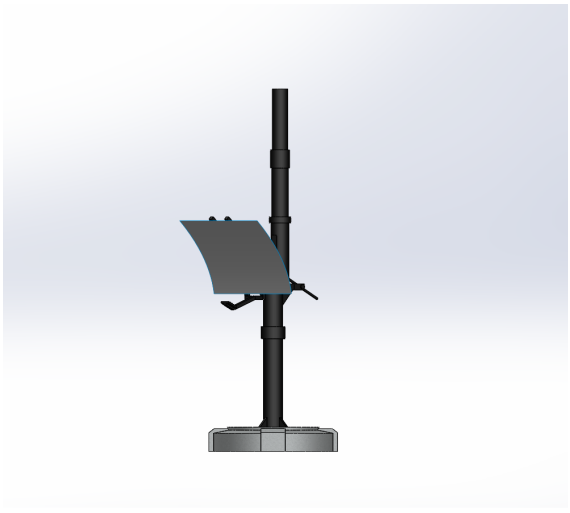

*Figure 4.2: Simplified relay station geometry, with only the reflector*

Upon completion, the models were exported in *.STEP* format and imported into *Microwave Studio* for electromagnetic simulation. The rover consists of three primary material categories, each assigned to specific structural components based on functional and electromagnetic considerations. The wheels are composed of Thermoplastic Polyurethane(TPU in red), selected for its mechanical

flexibility [27]. The main chassis, arm, drill assembly, and body structure are constructed from aluminum(Al in grey), a common aerospace-grade conductive material [28]. The camera housing, antenna support of the rover and the relay station structures are made from Carbon-fiber-reinforced polymer(CFRB in black)[29].

Detailed material properties, including permittivity, conductivity, and mechanical characteristics, are provided in *Appendix 8.4* as part of the bill of materials(BOM) used in the simulation environment.

## 4.3 Terrain Modeling

To model the Martian surface with both visual and scientific fidelity, the open-source 3D graphics software *Blender* was utilized, chosen for its powerful procedural capabilities and suitability for rapid prototyping in scientific applications [30]. Blender's node-based workflow enables the creation of complex textures by combining multiple procedural layers, effectively replicating the distinctive geological features of the Martian landscape. These include impact craters, rocky outcrops, and aeolian formations resulting from wind erosion. The generated textures are then applied to a displacement modifier, which algorithmically deforms the mesh to produce realistic surface irregularities(such as bumps, ridges, and depressions) without the need for manual sculpting.

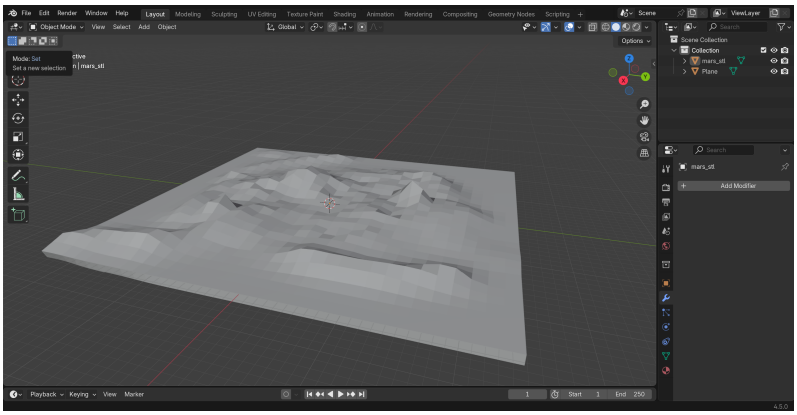

*Figure 4.3: Initial Martian terrain model generated in Blender*

Upon completion of the terrain model, the geometry was exported in *.STL* format and subsequently imported into SolidWorks 2025. Within SolidWorks, the file was converted to the *.STEP* format is a widely supported standard for geometry exchange in engineering simulation platforms. This *.STEP* file was then imported into Microwave Studio to be used in electromagnetic simulations.

Within the simulation environment, the terrain was assigned the dielectric properties of *Sandy Soil (dry)*, chosen to approximate the electromagnetic behavior of Martian regolith. The material properties used in the simulation are detailed in *Appendix 8.4*. To maintain computational efficiency while preserving realistic environmental features, the final terrain model was constrained to a $50 \times 50$ m footprint with modest surface deformations. This ensured a predominantly flat platform while still capturing the subtle undulations representative of the Martian surface.

## 4.4 Simulation Metrics and Evaluation Criteria

This section presents the physical parameters and performance criteria used to evaluate the electromagnetic behavior of the rover–station communication system, as introduced in *Chapter 3: System Overview and Communication Requirements*. Each communication link is evaluated using a set of key metrics that reflect its operational reliability, available bandwidth, and radiation efficiency within the simulated Martian environment.

While these metrics collectively provide insight into the system's electromagnetic performance, the evaluation of transmission power is treated separately. This aspect is analyzed using the theoretical framework established in *Section 2.2.5: Transmission Power*, where analytical models are applied to compare the required and achievable power levels under ideal and non-ideal conditions.

### 4.4.1 Return Loss, Impedance Matching and Radiation Pattern in Free Space

The return loss is used to assess impedance matching at the antenna feed point. A well-matched antenna exhibits values below $-10dB$ across the operational frequency band, indicating that less than 10% of incident power is reflected toward the source [31]. This is critical for minimizing signal losses and ensuring the simulated antenna performance aligns with real-world operating conditions.

For each antenna configuration in free space, frequency-domain or integral-solver simulations are performed to extract the $S_{1,1}$-parameter profile, with frequency taken from 0.1 to 10 GHz.

Following the impedance analysis, the subsequent phase involves evaluating the far-field radiation characteristics of the antennas in free space. This step is essential for establishing a reference baseline of antenna performance in an ideal, unobstructed environment. The resulting far-field patterns serve as a foundational framework for subsequent simulations, in which the antennas are integrated with the rover and Martian ground model. By characterizing the intrinsic radiation behavior in isolation, it becomes possible to identify and quantify the effects introduced by environmental and structural interactions in later stages of the analysis.

### 4.4.2 Radiation Pattern and Far-Field Directivity and Gain

A comprehensive analysis of the far-field radiation pattern under both free-space and realistic ground conditions is essential for accurately evaluating antenna performance. In free-space simulations, the antenna operates without any external interference, offering a clean reference point for key parameters such as beamwidth, peak directivity, and sidelobe structure. This idealised environment serves as a baseline for understanding the antenna's inherent radiation characteristics, free from the complexities introduced by real-world surroundings.

However, in practical scenarios, the presence of the ground introduces reflections that can significantly distort the radiation pattern. These effects are especially relevant in the far-field region, where the radiated wavefront has fully formed and stabilised. At this stage, ground-induced interference, primarily due to the interaction between direct and reflected waves, can either enhance or degrade signal strength at different angles, depending on whether the interference is constructive or destructive. Understanding these variations is crucial for predicting how the antenna will behave during real deployment.

By comparing the free-space and ground-influenced far-field patterns, it becomes possible to identify both the benefits and drawbacks introduced by environmental factors. This comparison is particularly important in mobile communication scenarios, such as rover-to-base station links, where the antenna must deliver consistent, omnidirectional coverage despite changes in orientation and position. To capture a more realistic picture of performance over varied terrain, the received signal on the rover is averaged across five different ground positions, as illustrated in *Figure 4.4*. This approach helps account for multipath and shadowing effects that may fluctuate with the rover's movement.

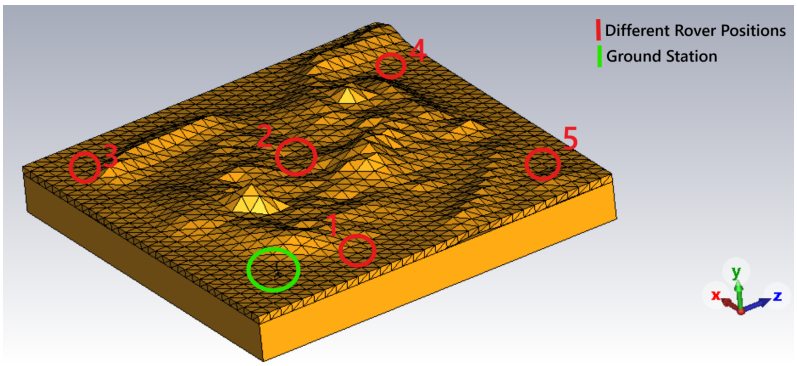


*Figure 4.4: The five distinct positions of the rover over realistic ground*

# Chapter 5: Simulation Results for the Omnidirectional-Omnidirectional System

## 5.1 2.4 GHz Omnidirectional Antenna Geometry

The radiating element for a 2.4GHz($\lambda \approx 12.50$ cm) in this section has been modeled as a vertically oriented cylindrical wire made of a PEC(Perfect Electric Conductor), with the initial dimensions shown in *Figure 5.1.*

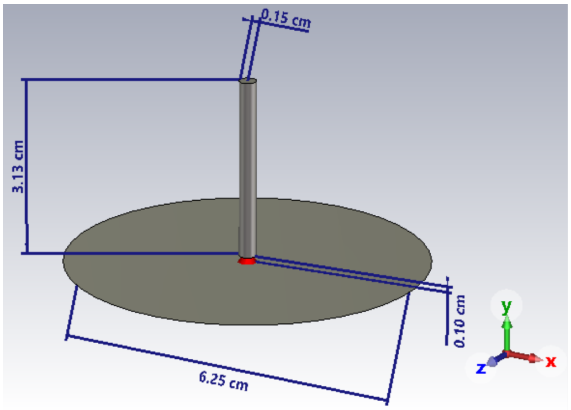


*Figure 5.1: The 3D design of the quarter-monopole antenna at 2.4 GHz with its dimensions*

This geometry would suggest that the antenna should resonate at a center frequency of 2.4GHz, following the theoretical predictions from *2.3.2: Quarter-Monopole Antennas.*

Excitation is provided through a discrete port located at the feed point of the antenna, across the 0.10 cm gap that electrically isolates the monopole from the ground plane. This arrangement closely approximates a coaxial feed, where the inner conductor is connected to the radiating element, and the outer conductor is connected to the ground plane. The discrete port not only provides a realistic excitation mechanism but also facilitates accurate computation of the antenna's input reflection coefficient by defining a reference impedance of 50 Ω for $S_{11}$ parameter analysis.

## 5.2 2.4GHz Omnidirectional Antenna in Free Space

### 5.2.1 S-parameter Analysis at 2.4 GHz

In theory, a monopole over an infinite ground should resonate when its physical length is around $\lambda/4$. The initial length of 3.13 cm was very close to the required length of $\lambda/4$; still, as seen in *Figure 5.2*, several factors caused the resonant frequency and impedance to deviate from the ideal, such as the used finite ground plane size and the neglect of end-effect adjustments. These factors made the antenna's electrical length and feed impedance different from the simple textbook values, resulting in a resonance that did not occur precisely at 2.4 GHz.

| Parameter | S11(1) | S11(12) |
|---|---|---|
| Length(l[cm]) | 3.13 | 3.30 |
| Radius(r[cm]) | 0.15 | 0.63 |
| Ground Plane Diameter(g[cm]) | 6.25 | 6.75 |
| Resonance[GHz] | 5.90 | 2.42 |
| S11[dB] at 2.4GHz | -6.7 | -42.28 |

*Table 5.1: Results from Figure 5.2 for S11(1) and S11(12)*

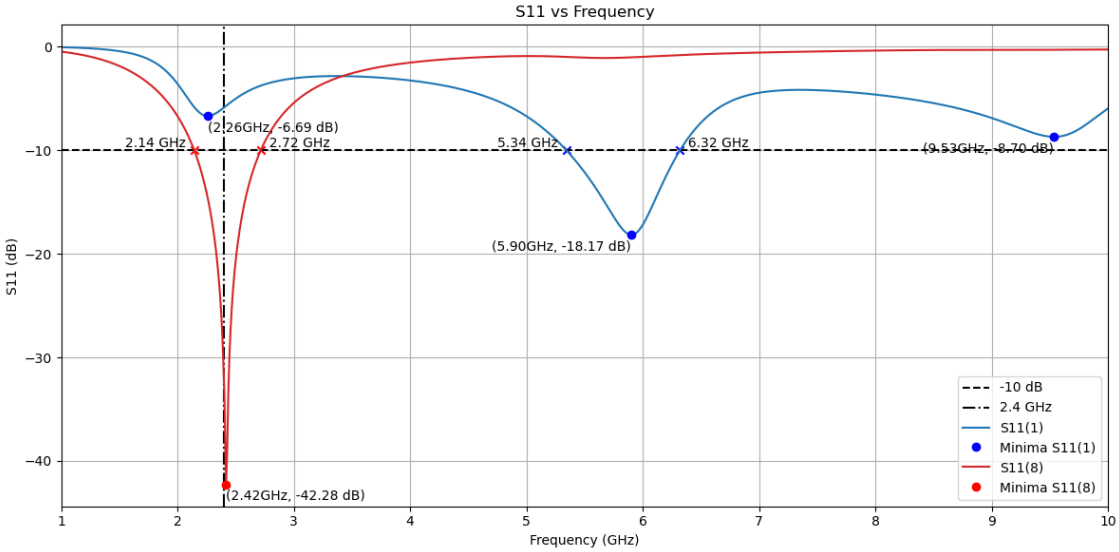


*Figure 5.2: Return loss (S11) vs. frequency for the initial and optimized quarter-wave monopole designs. The modified design achieves a sharp resonance at around 2.42 GHz(S11≈ −42 dB), whereas the initial design's resonance is offset around 2.26 GHz(S11≈ −6.69 dB - poor matching). The horizontal dashed line at -10 dB and the vertical line at 2.4GHz indicate the threshold and the target frequency band*

The simulation showed that the antenna's impedance was not purely resistive at 2.4 GHz(S11(1) occurred closer to 2.26 GHz), indicating the antenna was electrically a bit long for the frequency. By shortening the antenna length, it is possible to achieve resonance. However, another problem is encountered. The return loss achieved would still be under the desired -10 dB, meaning that more than 10% of the radiation is reflected, as stated in *2.2.3 The Scattering Parameter Matrix*, which is not ideal.

By analyzing S11(1) over a larger frequency domain in *Figure 5.2*, the antenna configuration seems to resonate better at 5.90 GHz. Therefore, instead of decreasing the length, the radius of the monopole was increased. A thicker monopole has a wider conductor, which increases the capacitance between the antenna and its surroundings(including the ground plane) and decreases the inductance per unit length [32]. This means a thick antenna appears electrically longer than a thin one of the same physical length. Consequently, by keeping the length constant, the thicker element will resonate at a lower frequency than 5.90 GHz.

By achieving the new resonance frequency of 2.78 GHz(*Figure 3* in *Appendix 8.4*), the antenna is still not resonant at 2.4 GHz, but now it indicates that the antenna is too short. By slowly increasing the antenna length, the resonance of 2.42 GHz was achieved.

### 5.2.2 Radiation Pattern Analysis at 2.4 GHz

The simulated realized gain of the quarter-wave monopole at 2.4GHz is approximately 1.84dBi. This value is a bit lower than the theoretical peak gain of 5.2 dBi for a quarter-wave monopole over an infinite ground plane[33]. By using a significantly small ground plane, the realized gain of the antenna was impacted. The maximum gain falls on the lower end of expected values; however, this was expected since the quarter-wave monopole was designed on a finite ground.

In terms of the far-field, the radiation pattern in the 2D polar cuts in *Figure 5.3a* shows nearly identical vertical-plane patterns, indicating that the antenna radiates symmetrically in all directions. The 3D gain pattern in *Figure 5.3b* confirms the expected toroidal radiation distribution around the vertical monopole, with maximum gain in the horizontal plane and minimal radiation along the antenna's axis.

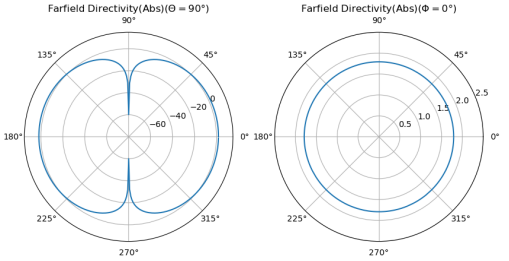


(a) The 2D polar cuts left at $\theta = 90°$ and right at $\phi = 0°$

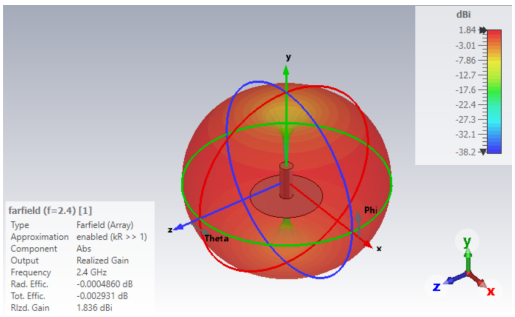


(b) The 3D realized gain pattern at maximum 1.84 dBi, including the $\theta$ and $\phi$ coordinate axes for angular reference

*Figure 5.3: The radiation characteristics of the quarter-monopole antenna at 2.4GHz*

Given these results, the antenna's radiation characteristics appear sufficient for testing on the rover. The omnidirectional pattern ought to ensure coverage around the rover in all directions, without wasting energy towards the sky, where it is not needed.

## 5.3 2.4GHz Omnidirectional Antenna on the Rover

In this section, to find the best position of the omnidirectional antenna, the antenna was placed in three distinct positions across the rover, and the far-field was analyzed, aiming to obtain the best radiation pattern, and compared it to the pattern obtained in free space.

### 5.3.1 Positioning of Antenna on the Rover

The three antenna placement approaches are illustrated in Figure 5.8b. These configurations include: an antenna mounted directly atop the rover's aluminum chassis(Position 1); an antenna elevated on a mast by 100 cm above the center of the rover chassis(Position 2); and an antenna situated 100 cm above one of the rear corners of the rover chassis(Position 3).

**Position 1**

Mounting the monopole antenna directly on the rover's aluminum chassis significantly alters its ideal omnidirectional radiation pattern, as demonstrated in Figure 5.5. The rover's large conductive structure, including its mechanical arm, acts as reflective and obstructive elements, thereby disturbing the inherent symmetry of the antenna's radiation pattern. Simulation results compared to the idealized free-space scenario indicate compromised radiation uniformity, resulting in the antenna no longer radiating equally in all directions.

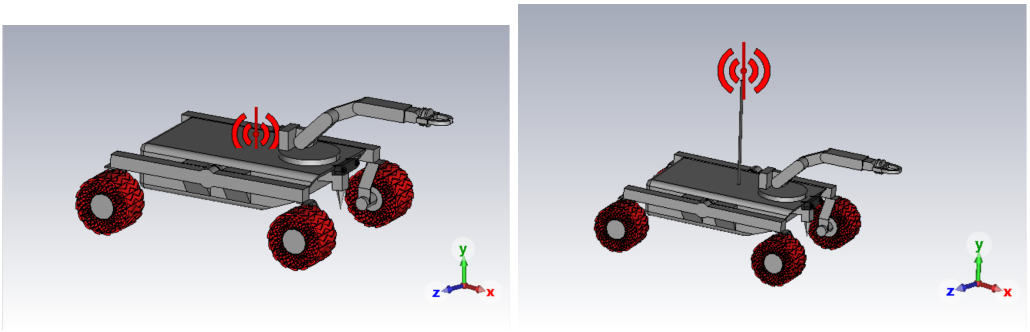

(a) Position 1: Chassis-Mounted

(b) Position 2: Mast-Central, 100 cm elevation

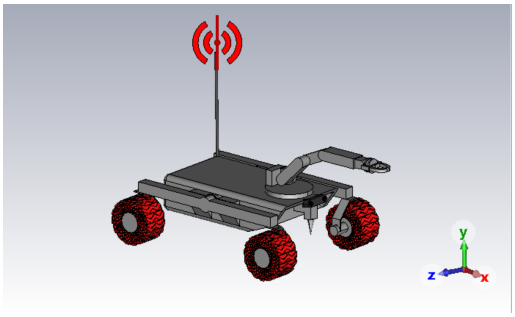

(c) Position 3: Mast-Rear 100 cm elevation

*Figure 5.4: The three distinct antenna positions across the rover*

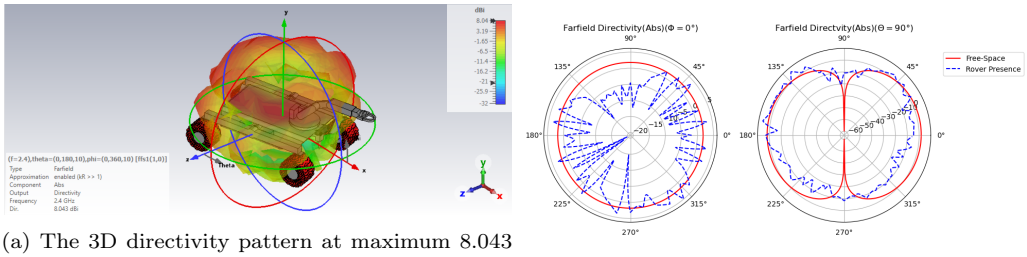


(a) The 3D directivity pattern at maximum 8.043 dBi

(b) The 2D polar coordinates

*Figure 5.5: The radiation characteristics of the antenna at Position 1*

**Position 2**

Elevating the antenna by 100 cm from the rover's chassis partially mitigates the distortion in the radiation pattern observed in *5.3.1 Position 1*. The polar radiation plot for $\phi = 0°$ depicted in *Figure 5.6b* clearly illustrates a pronounced null, likely attributable to the proximity and orientation of the rover's mast or arm structure.

**Position 3**

By relocating the antenna further towards the rear corner and maintaining an elevation of 100 cm, the simulations indicate improved radiation performance in the azimuthal plane ($\phi$ plane). Nevertheless, this configuration introduces new interference, with the rover body significantly blocking radiation in the elevation plane, as clearly visible at $\theta = 90°$ in *Figure 5.7b*. Thus, while mitigating some of the issues encountered in previous configurations, *Position 3* introduces significant blockage due to the antenna's proximity to the rover's larger structural components.

Given the suboptimal radiation patterns identified in all evaluated positions, a subsequent approach involves incorporating a second antenna positioned at a quarter-wavelength($\lambda/4$) spacing, maintained in-phase and amplitude, relative to the initial antenna. This arrangement aims to enhance reception capabilities and achieve improved omnidirectional radiation performance.

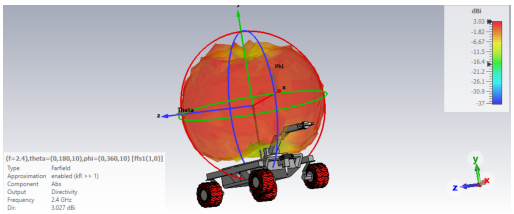

(a) The 3D directivity pattern at maximum 3.027 dBi

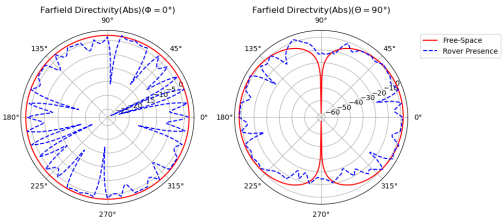


(b) The 2D polar coordinates

*Figure 5.6: Radiation characteristics for Position 2*

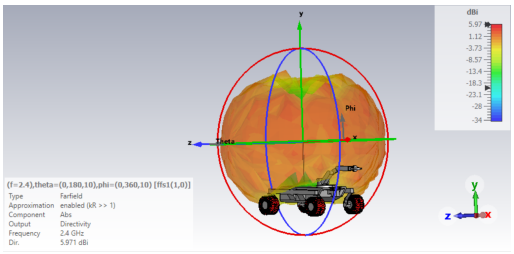

(a) The 3D directivity pattern at maximum 5.971 dBi

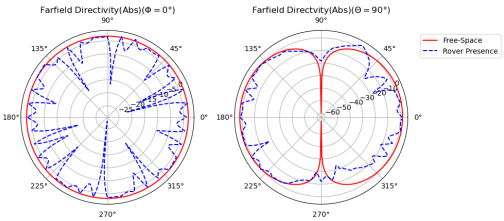


(b) The 2D polar coordinates

*Figure 5.7: The radiation characteristics of the antenna at Position 3*

### 5.3.2 Antennas in Amplitude on the Rover

Based on the previously presented results, *5.3.1 Position 2* exhibited the most favorable radiation pattern. Consequently, this position was chosen as the reference point for the placement of the antennas, to further analyze the amplitude characteristics of the antenna system.

Examining the polar coordinate plots depicted in *Figure 5.9*, it is evident that introducing a second antenna has not substantially enhanced the radiation pattern in the azimuthal plane. However, a notable improvement is observed in the elevation plane, where the mechanical arm no longer significantly obstructs radiation.

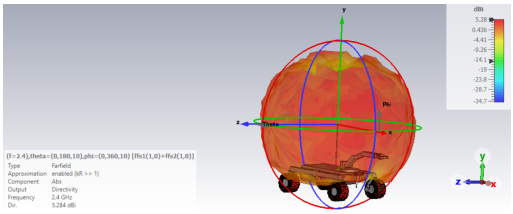

(a) The 3D directivity pattern at maximum 5.284 dBi

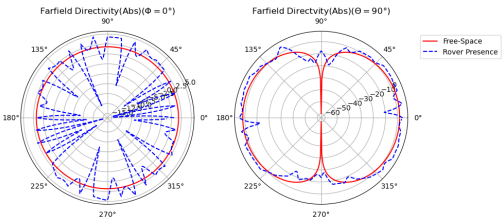


(b) The 2D polar coordinates

*Figure 5.8: The radiation characteristics of the antennas in amplitude at Position 2*

Overall, incorporating the second antenna has slightly improved the system's radiation characteristics, thus validating its use over five different positions in the following section.

### 5.3.3 2.4GHz Rover Average Signal

As discussed in *4.4.2 Radiation Pattern, Far-Field Gain, and Power Transmission in Non-Ideal Scenarios*, a comprehensive evaluation of antenna performance involves calculating the average signal across five distinct rover positions over the ground.

*Figure 5.9* illustrates that antennas mounted on the rover exhibit notable variations in gain around the polar planes. Specifically, in the plane defined by $\theta = 90°$, the far-field average radiation pattern still demonstrates reductions below the idealized free-space pattern. This reduction, as stated before, is a result of interference by the rover structure and the surrounding ground, disrupting the otherwise ideal omnidirectional radiation profile. Contrary to this, in the plane defined by $\phi = 0°$ (perpendicular to the rover's mechanical arm), the radiation pattern more closely approximates the free-space scenario, suggesting the antenna maintains relatively symmetrical radiation coverage in planes unaffected by structural interference. Observed discrepancies in this plane are predominantly attributable to the finite dimensions and geometry of the chassis, which acts as a ground plane.

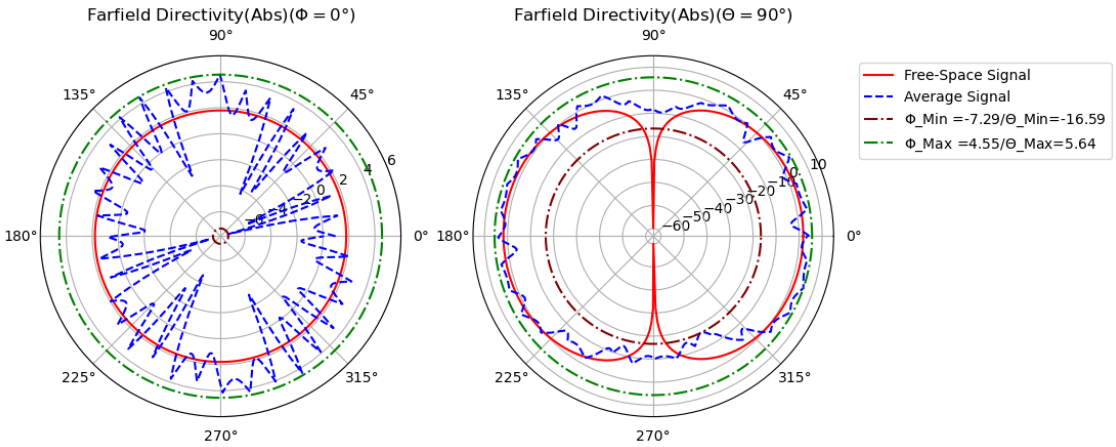


*Figure 5.9: 2D Polar coordinates showing:free space and the average signal over five positions of the rover, with the minima and and maxima*

## 5.4 2.4GHz Omnidirectional Antenna at Base Station

Analyzing the polar coordinate plots shown in *Figure 5.10c*, it becomes apparent that significant nulls in the azimuthal plane result from interference introduced by the ground and the relay mast. Additionally, a minor distortion is evident in the elevation plane. These distortions are not solely attributable to terrain or structural elements near the radiative component; they are also influenced by the presence of the PEC plane associated with the directional antenna operating at 5.8 GHz. This influence is confirmed by the three-dimensional far-field radiation pattern presented in *Figure 5.10b*, where distortion occurs away from the intended region of analysis. Consequently, given that the distortion does not significantly affect the primary area of interest, the resulting error is considered negligible for the current study.

## 5.5 Signal Power at 2.4 GHz

In this chapter, two distinct link budget calculations were conducted to evaluate the performance of the rover's communication system. Both analyses employ the *Friis Transmission Equation 2.8* to estimate the necessary transmit power, $P_t$, over a given distance, $R$. However, each calculation is based on different assumptions regarding antenna gains and receiver sensitivity.

The first calculation represents a minimal theoretical scenario. It assumes a highly constrained communication link characterized by an extremely narrow bandwidth (as specified in Table 3) and an idealized antenna gain of 5.16 dBi (approximately 3.28 in linear scale)[33]. This setup yields the absolute minimum transmitted power required to establish a viable communication link.

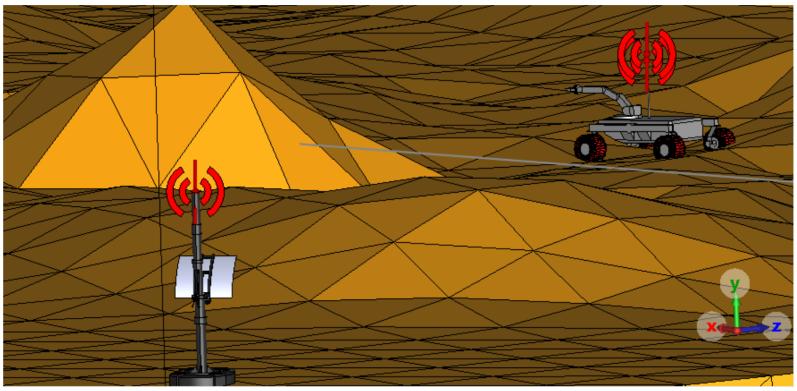

(a) Antenna position and the environment around

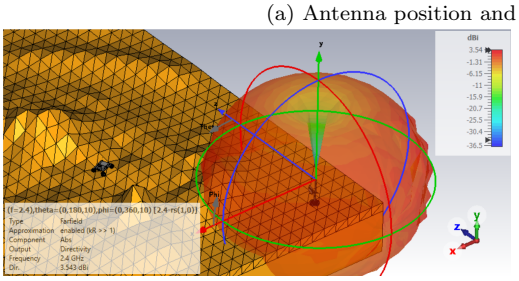

(b) The radiation characteristics of the antenna at the base station

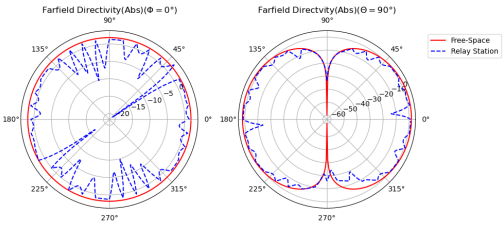


(c) The 2D polar coordinates

*Figure 5.10: Antenna analysis at relay station*

The second calculation incorporates realistic system parameters obtained through full-wave electromagnetic simulations. In this case, the antenna gains were derived from the directivity-based *Equation 2.9*, and the total efficiency of the antenna was reported by the simulation as -0.002931 dB (corresponding to a linear efficiency of approximately 0.99). The transmit antenna gain was determined to be $G_t = 5.27$ dBi (approximately 3.37 linear scale), and the receive antenna gain was $G_r = 5.96$ dBi (approximately 3.95 linear scale). This calculation also employed a more realistic value for the required receive power $P_r = 2.40 \times 10^{-12} W$ since the bandwidth here was 0.58 GHz calculated from the S11 graph in *Figure 5.2*, resulting in a higher estimated value for $P_t$, better reflecting the practical demands of the communication link.

| R[m] | $P_t(G_{t/r} = 5.16$ dBi)[W] | $P_t(G_t = 5.27$ dBi/$G_r = 5.96$ dBi)[W] |
|---|---|---|
| 10 | $4.37 \times 10^{-13}$ | $4.55 \times 10^{-8}$ |
| 25 | $2.73 \times 10^{-12}$ | $2.83 \times 10^{-7}$ |
| 50 | $1.09 \times 10^{-11}$ | $1.14 \times 10^{-6}$ |
| 100 | $4.37 \times 10^{-11}$ | $4.55 \times 10^{-5}$ |
| 1000 | $4.37 \times 10^{-9}$ | $4.55 \times 10^{-4}$ |
| 6000 | $1.57 \times 10^{-7}$ | $1.64 \times 10^{-2}$ |

*Table 5.2: Table of the values for the required transmitted power for the ideal and non-ideal case over five different distances for the 2.4 GHz System*

# Chapter 6: Simulation Results Omnidirectional-Directional System

## 6.1 5.8GHz Omni Antennas Geometry

The antenna described here operates at 5.8 GHz($\lambda \approx 5.17$ cm) and retains the same geometry as the 2.4 GHz omni antenna from *5.1 2.4 GHz Omnidirectional Antenna Geometry*, scaled to match the shorter wavelength.

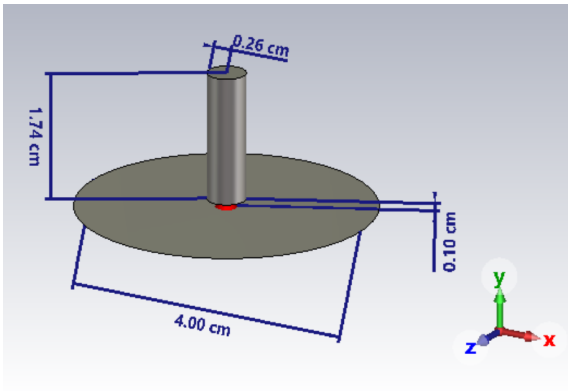


*Figure 6.1: The 3D design of the quarter-monopole antenna at 5.8 GHz with its dimensions*

## 6.2 Directional Antenna Geometry

### 6.2.1 Dipole Design

The fundamental radiating element of the directional antenna system is the *half-wavelength dipole*, previously introduced by the theory in section *2.3.1: Half-Wavelength Dipole*. This component defines the performance characteristics of the overall configuration, serving as the primary feed for the reflector structure.

The dipole's initial dimensions is constructed in *Figure 6.2*.

### 6.2.2 Plane Reflector Feed

To create the feed for the directional antenna, a plane made of PEC(Perfect Electric Conductor) has been introduced behind the dipole described in the previous chapter. Using the theoretical guidelines mentioned in *2.4.1: Plane Reflector*, the planer reflector has been modeled in textitFigure 6.3.

This chapter has outlined the geometry and placement strategy of the planar reflector. The integration of this feed into the parabolic reflector system will be explored in detail in the following sections.

### 6.2.3 Parabolic Plane Reflector with Off-Center Feed

To achieve a directive radiation pattern consistent with the HPBW specifications listed in *Table3*, a parabolic planar reflector geometry has been selected. This configuration is well-suited for focusing energy into a narrow beam in the $\phi$ plane, while offering a high opening in the $\theta$.

The physical dimensions of the reflector are bounded by the electromagnetic field region limits established in *2.2.2 Field Region*. Specifically, the lower bound is determined using the *Reactive Near-field Criterion*(*Equation 2.1*), while the upper bound is obtained from the *Fraunhofer Far-Field condition*(*Equation 2.3*). These constraints define a practical design range for the reflector

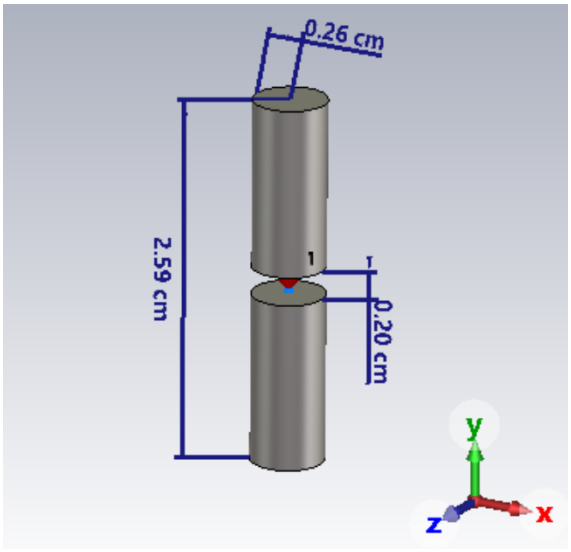


*Figure 6.2: The 3D design of the dipole antenna at 5.8 GHz with its dimensions*

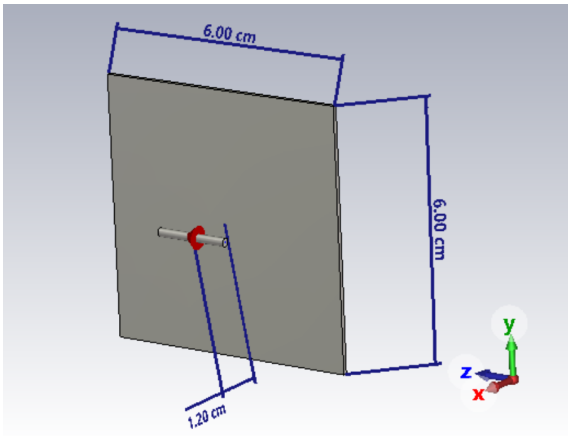


*Figure 6.3: Three-dimensional model of the dipole with planar reflector*

diameter $D$, expressed as:

$$\left[\lambda\left(\frac{R_1}{0.62}\right)^2\right]^{1/3} \leq D \leq \sqrt{\frac{R_2\lambda}{2}}$$

Assuming a near-field limit $R_1 = 2$ m and a far-field reference distance $R_2 = 50$ m, the allowable reflector diameter falls between approximately 81.33 cm and 113.69 cm. Based on this range, a reflector size of $90 \times 72$ cm is adopted for the design, providing a balance between spatial constraints and far-field performance.

Accurate placement of the feed element relative to the parabolic reflector is critical for optimal focusing and radiation efficiency. The first step in the alignment process involved calculating the focal point of the paraboloid. Based on a typical focal-to-diameter ratio of $f/D \approx 0.4$, the focal distance was determined to be 35 cm from the centre of the parabolic aperture.

To accommodate an off-axis feed arrangement(commonly used to minimise blockage in front of the reflector), the feed structure was displaced by 28 cm below the central axis of the paraboloid. This offset ensures that the feed remains aligned with the focal point while maintaining an unobstructed

reflective surface, enhancing the overall gain and beam symmetry.

A visual representation of the parabolic reflector with the offset feed configuration is provided in *Figure 6.4*.

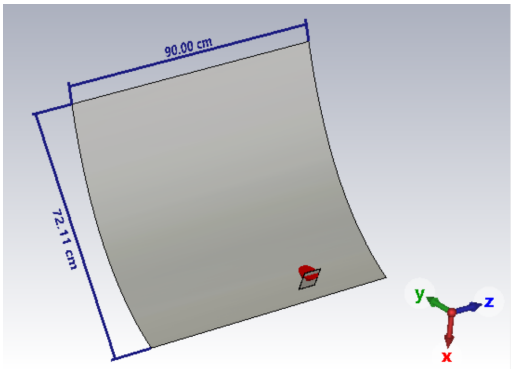


(a) Three-dimensional model of the parabolic reflector with off-axis feed

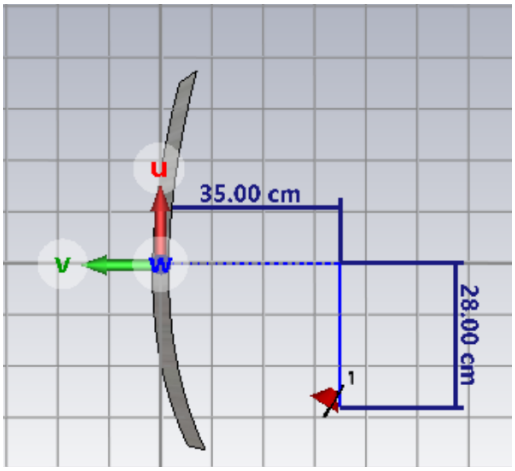


(b) Focal distance and feed displacement

*Figure 6.4: Parabolic reflector design with focal alignment and off-axis feed placement. The left panel shows the complete three-dimensional assembly, while the right panel highlights the focal length and feed displacement.*

## 6.3 5.8GHz Omnidirectional Antenna in Free Space

### 6.3.1 S-parameter analysis at 5.8 GHz Omnidirectional

The return loss analysis for the 5.8 GHz monopole antenna follows the same framework as discussed previously in section *5.2.1: S-Parameter Analysis at 2.4 GHz* for the 2.4 GHz design. However, deviations from ideal conditions resulted in a measurable shift in resonant behavior. In the initial simulation, the antenna exhibited a resonance at approximately 4.47 GHz, significantly below the target frequency of 5.8 GHz.

Despite this deviation, the simulated return loss remained above the acceptable threshold of -10 dB, indicating a need for parameter refinement of only the monopole's length and ground plane dimensions.

The capacitance between the monopole tip and the ground plane behaves similarly to that of a parallel-plate capacitor. A larger ground plane increases the effective capacitance, which causes the monopole to appear electrically longer, thereby lowering the resonant frequency. In the initial configuration, the ground plane was excessively large, contributing to the observed downward shift in resonance.

By reducing the ground plane size and making minor adjustments to the monopole length, the antenna was successfully tuned to resonate at 5.8 GHz. Although the final return loss value showed a slight increase in magnitude, it remained below the -10 dB threshold, indicating acceptable impedance matching and minimal reflected power.

### 6.3.2 Radiation Pattern

The simulated realized gain of the quarter-wave monopole at 5.8 GHz is approximately 1.47 dBi, which represents a reduction compared to the 2.4 GHz counterpart. This difference is primarily attributed to the relatively reduced ground plane used in the design.

The ground plane plays a critical role in shaping the performance of quarter-wave monopole antennas for real-life scenarios. A reduced ground size limits the reflective area available for

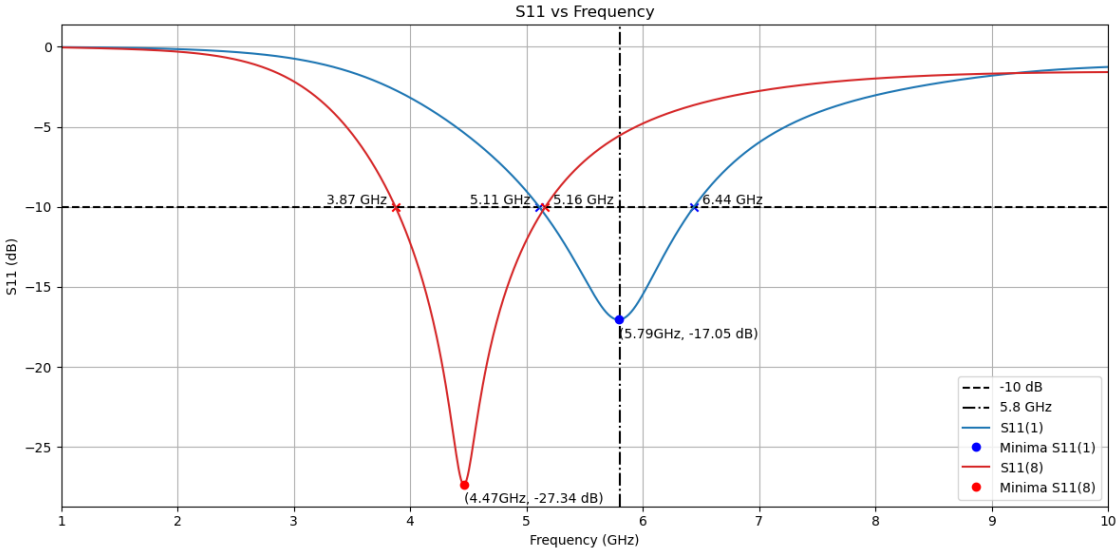


*Figure 6.5: Return loss (S11) vs. frequency for the initial and optimized quarter-wave monopole design. The modified design achieves a sharp resonance at around 5.79 GHz(S11≈ −17.05 dB), whereas the initial design's resonance is offset around 4.47 GHz(S11≈ −27.34 dB). The horizontal dashed line at -10 dB and the vertical line at 5.8 GHz indicate the threshold and the target frequency band*

| Parameter | S11(1) | S11(12) |
|---|---|---|
| Length(l[cm]) | 1.74 | 1.44 |
| Radius(r[cm]) | 0.26 | 0.26 |
| Ground Plane Diameter(g[cm]) | 4.00 | 2.59 |
| Resonance[GHz] | 4.47 | 5.79 |
| S11[dB] at 5.8GHz | -5.53 | -17.05 |

*Table 6.1: Results from Figure 5.2 for S11(1) and S11(8)*

constructive interference, resulting in diminished gain [34]. Consequently, the observed gain value is consistent with the previously set expectations.

Nonetheless, the radiation exhibits the omnidirectional toroidal pattern as seen in *Figure 6.6*. These results align with the reference patterns described earlier in section *5.2.2: Radiation Pattern Analysis at 2.4 GHz*. However, there are no indications of excessive loss or mismatch, so the slightly modest gain is attributed to the geometry rather than any design flaw.

## 6.4 5.8 GHz Directional Antenna in Free Space

### 6.4.1 S-Parameter Analysis at 5.8 GHz Dir

In the optimization of the directional antenna system, the return loss performance is predominantly governed by the characteristics of the dipole element. As the dipole is integrated into different subsystems, such as the planar reflector feed and the parabolic reflector, its electrical behavior is affected by changes in the surrounding structure.

To maintain resonance at the target frequency of 5.8 GHz, only the fundamental geometric parameters of the dipole were adjusted: namely, its length, radius, and the inter-element spacing between the dipole arms. These modifications ensure that the antenna remains properly matched to the desired frequency under varying environmental and structural configurations.

This approach of localized parameter tuning allows consistent impedance matching across all

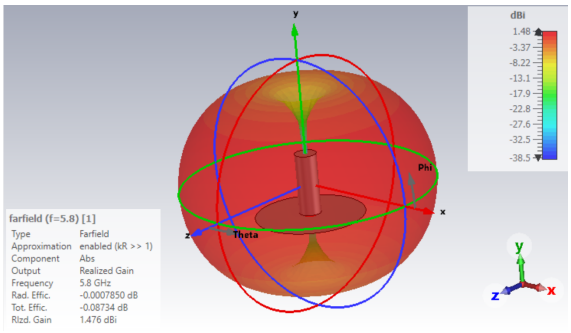


*Figure 6.6: The 3D realized gain pattern at maximum 1.47 dBi*

implementations of the dipole, thereby preserving efficient power transfer and minimizing reflected energy in each system context.

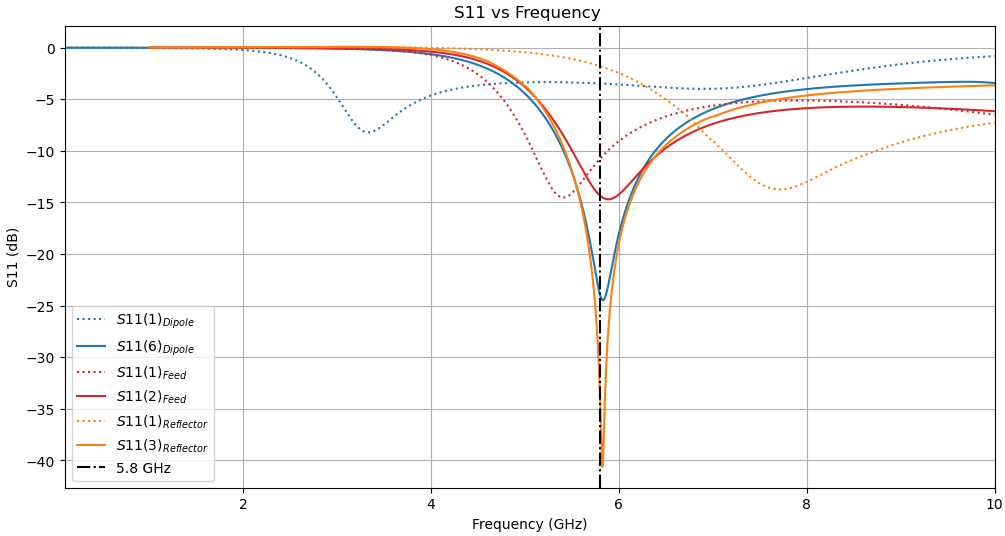


*Figure 6.7: Return loss (S11) vs. frequency for the initial(dotted line) and optimized(solid line) for the dipole, feed and reflector design. Each time the design has introduced the radiating element, the architecture of the dipole has been modified to resonate at 5.8 GHz*

| Parameter | $S11_D(1)$ | $S11_D(6)/S11_F(1)$ | $S11_F(2)/S11_R(1)$ | $S11_R(3)$ |
|---|---|---|---|---|
| Length(l[cm]) | 2.59 | 1.92 | 1.72 | 2.27 |
| Radius(r[cm]) | 0.26 | 0.10 | 0.10 | 0.10 |
| Arms Spacing(h[cm]) | 0.20 | 0.10 | 0.10 | 0.10 |

*Table 6.2: Table of the measurements of the dipole antenna for the graphs from Figure 6.7*

The optimization process began with an analysis of the dipole in free space. The theoretical size of the antenna leads to the parameter shown in *Table 6.2* for $S11_D(1)$. Initial simulation results revealed inadequate return loss performance, with values failing to meet the -10dB threshold typically required for acceptable impedance matching. To improve the return loss, the strategy was focused on increasing the capacitive coupling within the dipole structure.

The spacing between the arms influences capacitance in a dipole. By reducing the gap from 0.2 cm to 0.1 cm, the effective capacitance was increased, resulting in an improvement in return loss(intermediate result can be seen as S11(2) in *Figure 5* presented in *Appendix 8.4*).

As the design progressed toward full integration with the parabolic reflector system, attention shifted from isolated elements to the overall antenna configuration. The initial s-parameter response of the complete parabolic antenna is better visualized in *Figure 6.8*. In this configuration, the feed dipole had a length of 1.72 cm, which achieved resonance in the standalone feed structure, as observed in *Figure 6.7* for $S11(2)_{\text{Feed}}$. However, when incorporated into the parabolic assembly, this dipole length resulted in a resonance shift to approximately 7.71 GHz, indicating that the dipole was electrically too short in the context of the larger system. To compensate for this shift

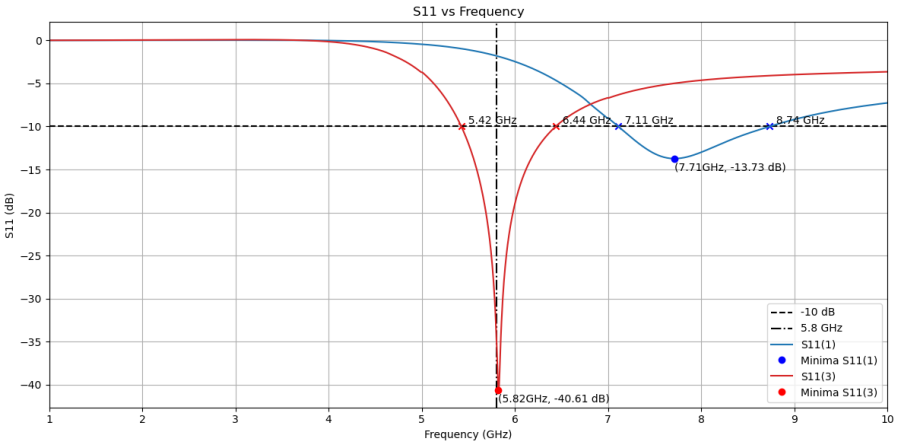


*Figure 6.8: Return loss (S11) vs. frequency for the initial and optimized directional antenna design. The modified design achieves a sharp resonance at around 5.82 GHz(S11≈ −40.61 dB), whereas the initial design's resonance is offset around 7.71 GHz(S11≈ −13.73 dB). The horizontal dashed line at -10 dB and the vertical line at 5.8 GHz indicate the threshold and the target frequency band*

and achieve resonance at the target frequency of 5.8 GHz, the dipole length was increased to 2.27 cm. This modification successfully restored the desired resonant behavior and improved the return loss to within acceptable limits.

### 6.4.2 Radiation Fields

For the rover's relay staion we are only intrested in the final parabolic reflector antenna, the realized gain will only be analyzed for that specific case, while for the dipole and feed subsystem, the radiation pattern will be analyzed for this two.

**Dipole Radiation Pattern**

The radiation pattern in the 2D polar cuts and 3D in *Figure 6.9*, show the expected shape that the dipole follows, with the negligible radiation along the antenna's axis.

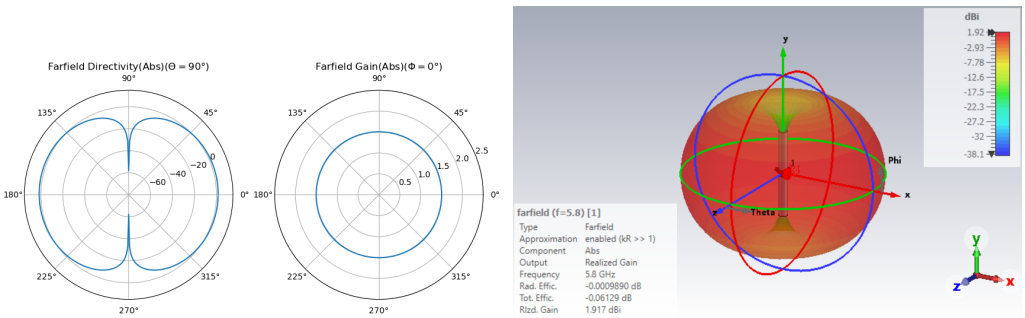


(a) The 2D polar cuts for the dipole field

(b) The 3D realized gain pattern at 1.91 dBi

*Figure 6.9: The radiation characteristics of the half-wavelength diopole antenna at 5.8GHz using 2D polar and 3D representations*

**Planar Reflector Feed Radiation Pattern**
When the dipole is placed in front of the PEC planar reflector, the radiation patterns shown in *Figure 6.10* result from the superposition of direct dipole emissions and reflections from the planar surface. In the $\phi = 0^\circ$ plot in *Figure 6.10a*, these rays interfere constructively, producing a strong main-lobe with high directivity and gain. At $\theta = 90^\circ$, the reflector forms sidelobes, and the nulls appear to be formed in the exact location as the dipole's.

In the 3D far-field rendering in *Figure 6.10b*, the main beam bulges forward, while radiation in the rear is suppressed. Side-lobes appear from angular regions where reflected and direct waves are out of phase. Overall, the planar reflector boosts the dipole's forward gain, making it ideal for a feed.

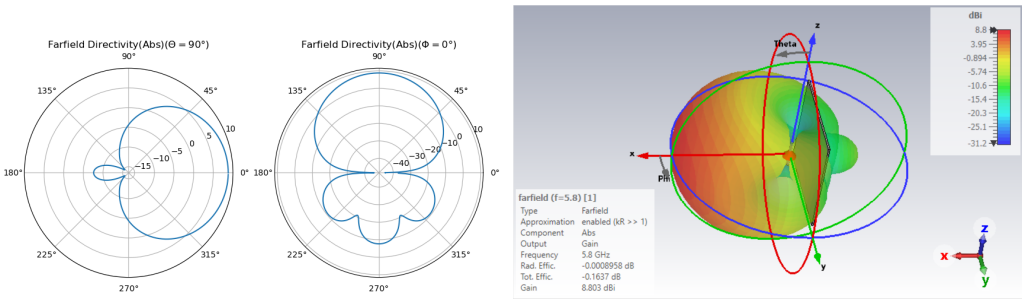


(a) The 2D polar cuts of the planar reflector feed (b) The 3D realized gain pattern at 5.80 dBi

*Figure 6.10: The radiation characteristics of the planar reflector feed antenna at 5.8GHz using 2D polar and 3D representations*

**Offset-Fed Square Parabolic Reflector Radiation Pattern**
The simulation results shown in *Figure 6.11* indicate that the antenna's beamwidth in both the horizontal and vertical planes is close to the intended design goals. The horizontal pattern (from *Figure 6.11a* ) shows an approximate HPBW on the order of around 150°. The simulated horizontal HPBW is falling 20° short of the intended angle of 170.85° described in *Table 3*, but the reflector is providing sufficient sector coverage. In the vertical plane (from *Figure 6.11b* ), the main lobe is much narrower. The vertical HPBW is around 50°, which aligns well with the 53.13°.

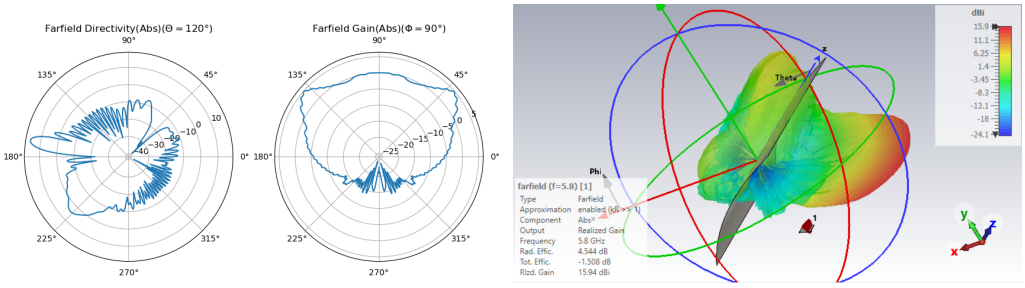


(a) The 2D polar cuts of the directional reflector (b) The 3D realized gain pattern at 15.94 dBi

*Figure 6.11: The radiation characteristics of the quarter-monopole antenna at 2.4GHz using 2D polar and 3D representations*

Crucially, the antenna's realized gain results show about 15.94 dBi. When compared with the literature, the antenna gain is performing a lot better than other wide-beam antennas, which only achieve 10–12 dBi gain for a beamwidth of around 150°[35].

## 6.5 5.8GHz Average Signal of Omnidirectional Antenna on the Rover

As established in *5.3 2.4GHz Rover Average Signal*, which examined the performance of the 2.4 GHz omnidirectional antenna mounted on the rover, the optimal radiation performance was achieved by

combining the outputs of two antennas in amplitude.

In this configuration, the antennas were elevated to a height of 110 cm above the rover chassis(10 cm higher than in the 2.4 GHz case to mitigate potential electromagnetic interference). As shown in Figure 6.12b, the resulting far-field radiation pattern demonstrates improved performance compared to the 2.4 GHz system. However, in the horizontal plane ($\theta = 90°$), the presence of the rover continues to induce pattern ripples, likely caused by multipath reflections between the rover structure and the ground.

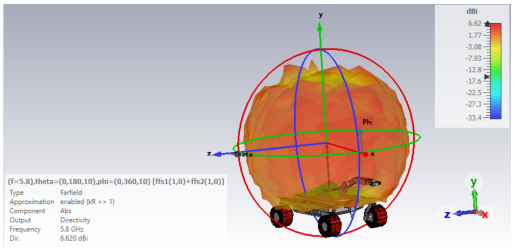

(a) The 3D directivity pattern at 6.62 dBi with the rover presence

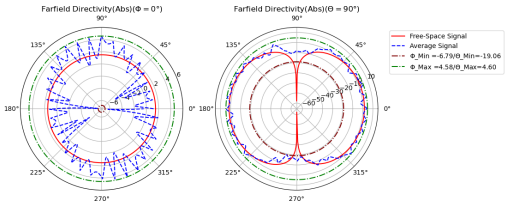


(b) The 2D polar plots

*Figure 6.12: Radiation characteristics for elevated dual-antenna configuration at 5.8GHz*

The primary limitation remains the shadowing effects introduced by the rover, which result in non-uniform azimuthal coverage. For robust and consistent communication, the antenna system must provide full 360° coverage, as the rover's orientation relative to the relay station may vary during operation. The simulation results indicate that, aside from specific shadowed sectors, the antenna maintains strong signal reception predominantly in the 90° and 270° azimuthal directions(lateral sides of the rover). In contrast, signal strength diminishes significantly near 0° and 180°(front and rear directions, respectively).

## 6.6 Directonal Antenna at Base Station

In the presence of a realistic ground below the antenna, as shown in *Figure 6.13b*, the peak directivity of the offset reflector is slightly increased relative to free space. This occurs because the ground acts like a reflector, adding an image source that constructively reinforces the main lobe in specific directions [36]. In the simulation, the maximum directivity reaches 20.28 dBi with ground, which shows an antenna gain improvement of almost 1.4 times the free space value.

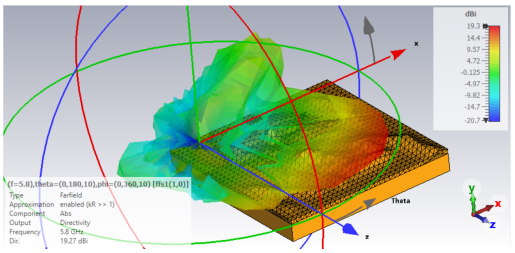

(a) The 3D directivity pattern at 20.28 dBi over realistic ground

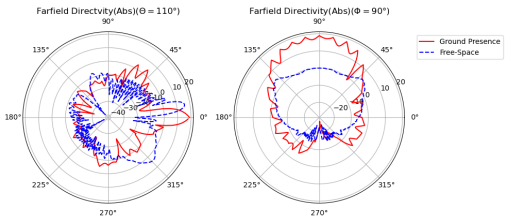


(b) The 2D polar plots

*Figure 6.13: Radiation characteristics for directional antenna configuration over realistic ground at 5.8GHz*

At the same time, the ground introduces deep nulls in the radiation pattern at certain angles, significantly reducing gain in those directions. As the red curve shows in *Figure 6.13a*, the directivity can drop to about -21.5 dBi in the worst null, a result of nearly complete destructive interference between the direct path and the ground. In contrast, the free-space pattern has no such nulls(aside

from the dish's normal sidelobes) because there is no reflective interference. This behavior can be explained by the two-ray interference theory, which states that the direct and reflected waves combine in-phase at some angles, can boost the gain, while out-of-phase waves would produce deep minima [36].

## 6.7 Signal Power

In this chapter, three distinct link budget calculations were conducted to evaluate the performance of the rover's communication system. All the data analyses employ the same calculations as in the previous section *5.5 Signal Power at 2.4 GHz*. The assumption here is that both systems are transceivers.

The first calculation represents a minimal theoretical scenario assumed for this link. It assumes a constrained communication link characterized by the video link bandwidth (as specified in Table 3) with the idealized quarter monopole gain at 5.16 dBi(approximately 3.28 in linear scale)[33], and the usual gain of 12 dBi(approximately 15.85 in linear scale) you would expect for a high spread farfield antenna [35].

The antenna gains were calculated in the same way as in the previous chapter, and their gains were: $G_{\text{Omni}} = 6.53$ dBi($\approx 4.50$ linear scale) and $G_{\text{Dir}} = 17.76$ dBi($\approx 59.73$ linear scale)

The second column assumes that the directional antenna acts as the receiver(omni-dir), therefore using *Figure 6.8* the bandwidth was approximated to be 1.02 GHz, with a receiver power of $4.22 \times 10^{-12} W$.

The third column assumes that the omnidirectional antenna acts as the receiver(dir-omni), therefore using *Figure 6.5* the bandwidth was approximated to be 1.28 GHz, with a receiver power of $5.30 \times 10^{-12} W$.

| R[m] | $P_t(G_t = 5.16$ dBi$/G_r = 12$ dBi)[W] | $P_t$(omni-dir)[W] | $P_t$(dir-omni)[W] |
|---|---|---|---|
| 10 | $8.83 \times 10^{-11}$ | $2.32 \times 10^{-8}$ | $2.9 \times 10^{-8}$ |
| 25 | $5.23 \times 10^{-10}$ | $5.79 \times 10^{-7}$ | $1.45 \times 10^{-7}$ |
| 50 | $2.21 \times 10^{-9}$ | $5.8 \times 10^{-7}$ | $7.28 \times 10^{-7}$ |
| 100 | $8.83 \times 10^{-9}$ | $2.32 \times 10^{-6}$ | $2.90 \times 10^{-6}$ |
| 1000 | $8.83 \times 10^{-7}$ | $2.32 \times 10^{-4}$ | $2.90 \times 10^{-4}$ |
| 6000 | $3.53 \times 10^{-8}$ | $3.18 \times 10^{-3}$ | $1.05 \times 10^{-2}$ |

*Table 6.3: Table of the values for the required transmitted power for the ideal and non-ideal case over five different distances for the 5.8 GHz System*

# Chapter 7: System Evaluation

## 7.1 Impedance Matching and S-Parameter Analysis

Impedance matching results revealed that both frequency bands required careful tuning to achieve minimal reflection and optimal resonance. The 2.4 GHz monopole was successfully optimized to achieve a return loss of approximately -42dB, while the 5.8 GHz monopole and directional antenna achieved return losses of -17 dB and -40 dB, respectively. These values indicate high power transfer efficiency across the system, ensuring that little transmitted energy is wasted or reflected into the feed line.

## 7.2 Antenna Positioning Strategies: Gains and Limitations

The study explored several positioning strategies for both the 2.4 GHz control antenna and the 5.8 GHz video link, each with distinct gains and limitations. For the 2.4 GHz omnidirectional antenna, three rover-mount configurations were evaluated.

### 7.2.1 Antenna Strategies for 2.4GHz on the Rover

*5.3.1 Position 1*(Chassis-Mounted) produced the highest peak gain(around 8.04 dBi) due to the chassis acting as an extended ground and reflector. However, this came with severe non-uniformity; many directions were attenuated by the rover's structure, undermining the 360° coverage.

*5.3.1 Position 2*(Mast-Central, 100cm elevation) yielded a much lower peak gain(around 3.02 dBi), since the antenna was farther from the conductive chassis and thus closer to a free-space monopole behavior. The benefit of *5.3.1 Position 2* was a more uniform azimuthal pattern, though a notable null persisted due to the mast interference.

*5.3.1 Position 3*(Mast-Rear, 100cm elevation) provided an intermediate peak gain(around 5.97 dBi). Its pattern coverage was better in the lateral directions but suffered from substantial blocking toward the front of the rover because the antenna was near one edge of the vehicle.

Each of these strategies involves a trade-off between gain and uniform coverage: mounting directly on the rover boosts gain via constructive reflections but at the cost of deep nulls, while elevating the antenna restores uniformity but can lower the net gain and introduce specific nulls from the antenna support.

Building on these findings, the dual-antenna strategy was implemented as an additional positioning approach. By placing a second 2.4 GHz antenna at quarter-wavelength distance on the mast in *5.3.1 Position 2* and feeding it in phase with the first, the design sought to fill coverage gaps. This dual setup (illustrated in *Figure 5.8*) achieved a peak gain of about 5.28 dBi(higher than the singular antenna at *5.3.1 Position 2*), and more importantly, it smoothed out the elevation-plane pattern irregularities caused by the rover's arm. The azimuthal pattern remained similar, indicating that the two antennas did not significantly beamform in the horizontal plane (as expected for closely spaced omnidirectional antennas). However, improvement in the vertical plane was evident, with the previously strong obstruction from the arm largely mitigated.

### 7.2.2 Antenna Strategies for 5.8GHz on the Rover

For the 5.8 GHz video link, the rover's antenna strategy likewise favored an elevated dual-antenna configuration. Two quarter-wave monopoles scaled for 5.8 GHz were mounted 110 cm above the chassis. This elevation was chosen to counteract the higher susceptibility of 5.8 GHz signals to blockage and near-field interference. The resulting radiation pattern, shown in *Figure 6.12*, had a peak directivity of about 6.62 dBi with the rover present. This is a notable gain increase compared to a single 5.8 GHz monopole in free space which only achieved 1.47 dBi), indicating that the combination of dual antennas and the rover's partial reflections provided a degree of gain enhancement.

The pattern for the 5.8 GHz system was generally improved over the 2.4 GHz system case in terms of gain and coverage. Nonetheless, it still exhibited ripples in the azimuthal plane due to multipath between the rover and the ground, and it suffered from shadowing in certain directions. Specifically, the front and rear (0° and 180° respectively) of the rover saw significantly reduced signal strength. However, the lateral sides(90° and 270°) had strong reception, implying that the antennas had a clear view in those directions.

## 7.3 Dual-Antenna Redundancy and Signal Stability

A key strategy in the rover's communication design was the use of redundant dual-antenna systems to enhance signal stability. By deploying two antennas in a combined configuration (fed in-phase and with equal amplitude), the system aimed to compensate for signal dropouts caused by rover orientation or obstructions. Simulation results confirmed that adding a second 2.4 GHz monopole yielded a modest but tangible improvement in coverage uniformity. In particular, while the dual-antenna setup did not dramatically alter the azimuthal radiation pattern, it significantly reduced the severity of vertical-plane nulls caused by the rover's mechanical structures. This indicates that the redundant antenna provided alternative propagation paths when one antenna's signal was shadowed, stabilizing the overall link.

Consistently, the best radiation performance for the 5.8 GHz video link was also achieved using a dual-antenna configuration on the rover. In that case, two 5.8 GHz antennas elevated higher than the 2.4 GHz antennas above the rover chassis were combined, effectively enhancing signal stability through spatial diversity and redundancy, mitigating the risk of communication blackouts when the rover's orientation or environment might block one of the communication systems. This redundancy is crucial for a Martian rover, as continuous control and data links must be maintained even if one antenna experiences fading or obstruction.

## 7.4 Mutual Coupling and Mitigation Strategies

Introducing multiple antennas in close proximity naturally raises concerns about mutual coupling, which can detune antennas and distort their radiation patterns. In this project, careful attention was paid to antenna placement and feeding to minimize adverse coupling effects.

The two 2.4 GHz quarter-wave monopoles on the rover were spaced by approximately $\lambda/4$ and driven in phase. This configuration encourages constructive interference in desired directions while keeping the antennas relatively close. This spacing was a trade-off: a small separation improves combined omnidirectional coverage but can increase coupling. The results indicate that any mutual coupling between the redundant monopoles did not introduce severe pattern distortions; the elevation-plane coverage improved with the twin-antenna system.

One implicit mitigation strategy was the use of frequency separation: the control and video antennas operate at 2.4 GHz and 5.8 GHz, respectively, which inherently reduces mutual coupling between the two systems. The large frequency difference means each antenna is electrically small from the perspective of the other, limiting their interaction. Additionally, the antennas were placed at different heights (the 5.8 GHz antennas were mounted 10 cm higher than the 2.4 GHz ones) and also placed along their vertical axis(where a null would form on an omnidirectional antenna pattern) to further decouple them and avoid near-field interference. This vertical separation, alongside careful routing of feed lines and possibly shielding of the high-gain 5.8 GHz antenna's ground plane, helped mitigate coupling.

Minor distortion was observed in the 2.4 GHz base-station antenna's pattern due to the presence of the nearby 5.8 GHz directional antenna's metallic structure. However, this effect was localized outside the primary service area and deemed negligible for operation. Overall, by combining spatial separation, orthogonal placement of different-frequency antennas, and in-phase feeding of same-frequency antennas, the design minimized mutual coupling and ensured that the performance of each link remained largely independent and optimal.

## 7.5 Combined Performance of the communication systems Links

Evaluating both links under realistic operational scenarios reveals that the integrated communication system meets its design objectives.

### 7.5.1 Performance of the Control(2.4GHz) System

With its omnidirectional rover antennas and an omnidirectional base antenna, demonstrated reliable coverage around the rover with an average radiation performance somewhat below the ideal due to environmental factors. When averaged over five different rover positions (to simulate various orientations and locations of the rover), the 2.4 GHz antenna's radiation pattern still showed dips in gain relative to free space, particularly in the horizontal plane. These reductions were attributed to interference from the rover chassis and the ground, as discussed earlier. In planes less affected by the rover structure, the 2.4 GHz pattern more closely resembled the free-space case, indicating that the control link can maintain near-omnidirectional coverage except where the rover's structure acts as a shield. Importantly, by using the dual-antenna configuration for 2.4 GHz, the design achieved a measure of consistency in radiation in the elevation plane, reducing the risk of total signal loss as the rover pitches or rolls. This translates to a robust control link in practice, as the rover can be steered from virtually any direction around the base station with minimal risk of a sudden deep fade.

The theoretical and practical link budget scenarios were compared: in an idealized narrow-band case, the required transmit power at 100 m was on the order of $10^{-11}$ W, whereas with realistic bandwidth and simulated antenna gains it rose to about $10^{-5}$ W. This latter figure is still relatively low, illustrating that even with conservative assumptions the 2.4 GHz link has a large link margin.

In fact, even at distances of up to 6 kilometers or more, the control link would require only milliwatts of required transmit power to remain operational. These values confirm that the rover's control channel is very robust under the chosen design, easily covering the expected operational range with substantial fade margin to spare.

### 7.5.2 Performance of the Video(5.8GHz) System

The video link had inherently more challenges; higher frequency signals suffer greater free-space path loss and are more easily blocked. With two 5.8 GHz monopoles on the rover and a high-gain directional antenna at the base station, the video link achieved strong signal levels in most directions except the immediate front and back of the rover. During realistic operations, the rover's orientation relative to the relay station will not always be optimal.

Due to its higher data rate and bandwidth, it naturally demands more power, but remains feasible. Using the measured antenna gains (approximately 6.5 dBi omnidirectional on the rover and 17.8 dBi for the base station reflector) and a realistic receiver sensitivity, the required transmit power was calculated for various distances. For example, at 100 m range with the rover transmitting via its omnidirectional antenna and the base station using the directional receiver(the omnidirectional-directional case), the link would require on the order of $10^{-6}$ W of required transmit power to achieve a reliable video feed. Even at 6 km, the necessary power remains on the order of milliwatts. The calculations also compared a hypothetical directional-omnidirectional case when the station would need to communicate with the rover. This scenario consistently required slightly higher required transmission powers for the same range, suggesting that even if the 2.4 GHz system is undergoing blackouts, the 5.8 GHz system can be used for redundancy purposes.

In practice, the rover will transmit video omnidirectionally (easing the need for active pointing on a moving rover), while the base station's high-gain dish will be pointed at the rover to receive. This configuration takes advantage of the base station's ability to host a larger, more directional antenna and the rover's need for simplicity and coverage.

## 7.6 Sensitivity to Ground Topography and Antenna Height

The Martian terrain and the height of antennas above ground play a crucial role in communication performance, primarily through their influence on multipath propagation and line-of-sight conditions.

The simulation results included a flat ground plane in the environment, which already revealed important sensitivity factors. For the base station's 5.8 GHz parabolic antenna, the presence of realistic ground dramatically altered the radiation pattern: it increased the peak directivity(from about 15.94 dBi in free space to 19.27 dBi with ground) by adding a constructive image source, but simultaneously introduced deep nulls at certain elevation angles due to the two-ray interference effect. In the worst case, destructive interference between the direct and ground-reflected rays caused the directivity to drop as low as -20.7 dBi in specific directions. This phenomenon is susceptible to antenna height; if the antenna or the rover is at different elevations relative to the ground, the angles at which constructive or destructive interference occurs will shift. For instance, raising the base station antenna higher would generally push the first destructive interference null closer to the horizon(potentially beyond the rover's position), while lowering it could bring a null into the direct line-of-sight to the rover. The rover's motion over uneven Martian topography would further impact this: if the rover goes into a crater or behind a hill relative to the base, the ground reflection geometry changes and can either alleviate or worsen the interference. Thus, maintaining sufficient antenna height and, where possible, a clear line of sight above ground obstructions is critical for consistent communication.

Increasing antenna height proved to be a straightforward and effective way to mitigate some ground-related issues. That extra 10 cm elevation from the 5.8 GHz system contributed to a cleaner radiation pattern(with slightly reduced ground-induced nulls). Height is even more influential at longer ranges.

As distance increases, the angle to the rover from the base station becomes smaller, so the risk of the rover falling into a ground interference null is greater if the antennas are low. This issue was mitigated by placing the radiating elements from the relay station at the proper heights(monopole antenna at 3 m high and the reflector at 1.5 m).

# Chapter 8: Conclusion and Further Improvements

This study has critically evaluated the performance of a dual-band communication system for a Martian rover, integrating both 2.4 GHz and 5.8 GHz links to support control and high-bandwidth video transmission, respectively. Through the simulation-based platform *CST Microwave Studio Suite* analysis of antenna characteristics, system geometry, environmental factors, and interlink interference, the study has shown that the system design satisfies core performance objectives and offers a viable approach to robust communications.

## 8.1 Summary of Key Findings

The following points summarize the development, optimization, and integration of the antenna systems for the rover. They outline key stages in the design process, highlight the challenges encountered during implementation, and demonstrate how practical adjustments and empirical validation ensured reliable performance for both control and video transmission links under realistic operating conditions:

- The initial antenna designs matched theoretical resonance closely, but practical factors (limited ground size or end effects) caused significant detuning. Iterative tuning optimized resonance at 2.42 GHz (–42.28 dB) and 5.82 GHz (–40.61 dB), underscoring the need for empirical or simulation-based refinement beyond textbook models in complex environments.
- After tuning, the antennas were integrated into the rover to optimize omnidirectional coverage under real conditions. Tests of single-antenna placements(mounted on the chassis, central mast, and rear corner) showed uneven radiation due to structural interference and ground reflections.
- The uneven radiation structure was addressed by adding a second antenna placed in phase and with matched amplitude relative to the original. The elevated dual-omnidirectional antenna setup provided moderate gain and broad azimuthal coverage, but could not fully eliminate front and rear gaps caused by the rover's bulk. Since all placement options had trade-offs, the final design balanced elevation, diversity, and positioning to meet communication needs.
- Operating the control and video links on widely separated frequency bands (2.4 GHz and 5.8 GHz) proved to be an effective means of interference reduction. This frequency separation ensured that each link did not directly interfere with the other's signals, allowing simultaneous operation without significant co-channel interference.
- The antennas were physically separated to reduce near-field interaction: the 5.8 GHz rover antennas was 10 cm above the 2.4 GHz one, and at the base station, the 5.8 GHz antenna was at 150 cm while the 2.4 GHz receiver was at 300 cm. Simulations showed minimal pattern distortion from nearby metallic structures, occurring outside the main communication sector and having negligible impact on the 2.4 GHz link.
- Control and video link analyses show strong performance under nominal conditions. The control link offers omnidirectional coverage with minimal power (down to $1.82 \times 10^{-7}$ W at 10 m), while the video link supports high-bandwidth transmission over long ranges (up to 6000 m) with high gain.

## 8.2 Practical Implementations of the systems

The implemented communication system simulations show enough robustness that it could be introduced in real life. The dual-antenna design on the rover improved reliability by reducing coverage gaps and preventing signal nulls, ensuring consistent connectivity during movement. Frequency separation(using 2.4 GHz for control and 5.8 GHz for video) allowed each link to be optimized for its purpose, with the control link benefiting from better propagation and the video

link leveraging higher bandwidth. A high-gain directional antenna at the base station, enhanced by ground reflections, provided 19.27 dBi gain, extending the video range significantly. Meanwhile, the rover's omnidirectional antennas offered broad coverage without the need for manual orientation. Finally, link budget analysis showed strong signal margins even under realistic multipath conditions, indicating robust performance well-suited for harsh environments like Mars.

## 8.3 Limitations and Potential Improvements

One of the main limitations of the simulated system came from the simulation environments, which when using the Frequency or Integral Solvers over a more complex setting(rover presence or the ground), The speed of the simulation was increased by an exorbitant amount(could be up to more than a day) due to the number of meshes that can be distributed over the system. CST needs several mesh cells per material period to correctly model the shape of the elements and the fields and currents. This works out to a large number of mesh cells per wavelength. This is usually more than the density required for modeling simple monopole antennas or a waveguide at the same frequency. The rover, ground, and the ground station with the additional antennas each would probably need at least 10 by 10 mesh cells in each layer, so the number of mesh cells is about 60000 times the number of mesh cells in the thickness. This comes close to more than a million. CST sends a pulse into the mesh and looks at the multiple reflections. For one edge to interact with the opposite edge of the arrangement, the pulse must travel through more than 240 mesh cells and back. It would take several bounces to settle close to the right answer, so it needs to calculate the fields at a million points several thousand times before it has the correct answer. Therefore, unfortunately, it was not possible to directly capture mutual coupling or leakage between channels since this requires obtaining the graph for the S12/21, which are not implemented into the *Asyptotic Solver* of *Microwave Studio*, which was used for farfield analysis.

Despite the mid-success of the simulations, the design has some limitations that invite improvement. A primary limitation is the residual pattern non-uniformity and shadowing caused by the rover itself. The results highlight that certain angles have significantly weakened signals due to the rover's body obstructing the line of sight. While the dual-antenna approach alleviated this to an extent, it did not eliminate it. A possible improvement could be to incorporate antennas on multiple parts of the rover. Future designs might explore optimized spacing or the addition of a neutralization line/decoupling network between the two antennas to improve isolation further and ensure that adding a second antenna does not detune the first.

One more area for improvement is the directivity of the rover's video transmitter. The current design kept it omnidirectional for simplicity, but that means a lot of transmitted power is wasted in directions where the base station is not located. If the rover's orientation can be roughly known or controlled, a moderate-gain patch can be added to on the rover for 5.8 GHz to concentrate energy toward the base station, improving link margin or allowing even higher data rates for the video.

Lastly, environmental factors such as Martian dust storms or extreme temperatures were outside the scope of the simulation, but in practice, they could affect signal propagation and hardware performance. A robust design might consider redundant frequency bands (also having an X-band link as backup) or error-correcting protocols to handle intermittent degradation.

## 8.4 Future Extensions

The ultimate goal would be to prototype the antennas at least for the Earth environment. To implement this antenna system in real life, the quarter-wave monopoles for both 2.4 GHz and 5.8 GHz would be constructed from conductive rods (copper or aluminum) mounted over ground planes, and placed on the rover as discussed in the two results section for antennas amplified on the rover.

The base station would host a high-gain 5.8 GHz directional antenna(a parabolic reflector) mounted 1.5-3 m high and aligned with the rover's operational area. All antennas would use coaxial feeds and be designed for protection from the Earth's outside environment. Redundant paths and diversity reception would be included to ensure robust communication in variable terrain and orientation.

# References


[1] Center for Astrophysics — Harvard & Smithsonian. Solar system. https://www.cfa.harvard.edu/research/topic/solar-system.

[2] Payal Dhar. How to build an internet on mars. https://study.com/academy/lesson/technologies-used-to-explore-space.html.

[3] European Space Agency. Why go to mars? https://www.esa.int/Science_Exploration/Human_and_Robotic_Exploration/Exploration/Why_go_to_Mars.

[4] Deimos Space. Why mars?, March 2021. https://deimos-space.com/mars-exploration.

[5] Elizabeth Howell. Lunokhod 1: 1st Successful Lunar Rover, December 2016. https://www.space.com/35090-lunokhod-1.html.

[6] Kelli Mars. 25 Years Ago: Mars Pathfinder Launches to Mars to Deploy Sojourner, the First Planetary Rover, 2021. https://www.nasa.gov/history/25-years-ago-mars-pathfinder-launches-to-mars-to-deploy-sojourner-the-first-planetary-rover/

[7] NASA Astrobiology Program. Mers–mars exploration rovers, 2025. https://astrobiology.nasa.gov/missions/mer/.

[8] NASA Science. Mars science laboratory: Curiosity rover, April 2025. https://science.nasa.gov/mission/msl-curiosity/.

[9] Space Ambition. The red frontier: Mars rover's legacy, 2024. https://spaceambition.substack.com/p/the-red-frontier-mars-rovers-legacy,.

[10] NASA Science. Three generations of rovers in mars yard, n.d. https://science.nasa.gov/resource/three-generations-of-rovers-in-mars-yard.

[11] NASA Science. Science instruments, n.d. https://science.nasa.gov/mission/msl-curiosity/science-instruments.

[12] Keerthi Chandrasekaran and Patrick M. Estabrook. Msl telecommunications system design. In *Deep Space Communications and Navigation Series*, DESCANSO Design and Performance Summary Series, chapter 7. Jet Propulsion Laboratory, California Institute of Technology, 2014. https://descanso.jpl.nasa.gov/monograph/series13/DeepCommo_Chapter7--141030.pdf.

[13] Carolyn Gramling. Mars needs internet: Laser links will help rovers talk to earth. *Science News*, 2024. https://www.sciencenews.org/article/mars-internet-communication-rover-psyche.

[14] Simon R. Saunders; Alejandro Aragon-Zavala. *Antennas and Propagation for Wireless Communication Systems*. JohnWiley Sons Ltd.; The Atrium, Southern Gate,, Chichester,West Sussex, PO19 8SQ, England, 2007.

[15] Constantine A. Balanis. *Antenna Theory Analysis and Design*. John Wiley Sons, Inc., 2016.

[16] A. Ali, R. Eid, D. E. Manaseer, H. K. AbuJaber, and A. Ware. Dual-band 802.11 rf energy harvesting optimization for iot devices with improved patch antenna design and impedance matching. *Sensors (Basel)*, 25(4):1055, Feb 2025. https://www.ncbi.nlm.nih.gov/pmc/articles/PMC11859205/.

[17] Scott Alan Geels. System design of a mars ascent vehicle, 1989. https://dspace.mit.edu/bitstream/handle/1721.1/42190/22926409-MIT.pdf?sequence=2&isAllowed=y.

[18] Olivier R. Hainaut. Signal, Noise and Detection, June 2005. https://www.eso.org/~ohainaut/ccd/sn.html.

[19] National Institute of Standards and Technology (NIST). Boltzmann constant $k$ — codata recommended value, 2025. https://physics.nist.gov/cgi-bin/cuu/Value?k.

[20] Satellite Signals Limited. Noise temperature, noise figure (nf) and noise factor (f), March 2025. https://www.satsig.net/noise.htm.

[21] Pengjian Gao, Jia Li, and Weibing Wang. Study of ground plane effects on monopole antenna performance. *Electronics*, 12(12):2681, 2023. https://www.mdpi.com/2079-9292/12/12/2681.

[22] Dassault Systemes. Simulia simulation software, 2025-05-29. https://www.3ds.com/products/simulia.

[23] GoEngineer. Cst studio suite 2025: Goengineer software buying guide. Software buying guide, GoEngineer, 2024. https://cdn.goengineer.com/cst-studio-suite-2025-goengineer-buying-guide.pdf.

[24] Dassault Systèmes. Electromagnetic simulation solvers. https://www.3ds.com/products/simulia/cst-studio-suite/electromagnetic-simulation-solvers.

[25] Alain-Paul Begaud. *CST Microwave Studio®: Advanced Topics Manual*. TELECOM Paris (formerly ENST), 2003. Online training manual for advanced users of CST Microwave Studio.

[26] Jupyter Team. Project jupyter documentation, 2015. https://docs.jupyter.org/en/latest/.

[27] Proto Labs, Inc. Tpu elastomer: Key benefits and advantages, n.d. https://www.protolabs.com/materials/tpu/, publisher = Proto Labs, Inc.

[28] European Space Agency. To see the Universe in aluminium, December 2023. https://www.esa.int/Enabling_Support/Space_Engineering_Technology/To_see_the_Universe_in_aluminium.

[29] Mitsubishi Chemical Corporation. Space Case Study: Carbon Fiber & Carbon Fiber Reinforced Plastics (CFRP) in Satellite Applications, n.d. https://www.m-chemical.co.jp/carbon-fiber/en/case/space/.

[30] Blender Foundation. Blender—home of the blender project, the free 3d creation suite. https://www.blender.org.

[31] Maxtena. Antenna specifications. https://maxtena.com/RFTools/AntennaSpecifications.

[32] Vishwanath Iyer, Shashank Kulkarni, Giorgia Zucchelli, and Sergey N. Makarov. Increasing the impedance bandwidth of dipole and monopole antennas with parasitic elements. In *2016 10th European Conference on Antennas and Propagation (EuCAP)*, pages 1–4, 2016.

[33] C. Logan J. and W. Rockway J.˙Dipole and Monopole Antenna Gain and Effective Area for Communication Formulas. Technical Report Technical Report 1756, Naval Command, Control and Ocean Surveillance Center RDT&E Division, San Diego, CA, September 1997. DTIC accession number ADA332891; approved for public release, distribution unlimited.

[34] Rapin Kudpik, Piyaphorn Meesawad, and Rangsan Wongsan. Performance improvement for monopole antenna with circumferential wire medium. In *Proceedings of the 2018 International Symposium on Antennas and Propagation (ISAP 2018)*, page 459, Busan, South Korea, October 2018. Paper FRF2-1.

[35] Zhenhua Li Bin Wang and Shufei Yin. A wide-beam antenna for automotive radar based on improved particle swarm algorithm. In *International Journal of Automotive Manufacturing and*

*Materials IJAMM*, 2024. https://www.sciltp.com/journals/ijamm/article/download/517/316/3008#:~:text=24,planar%20array%20with%20wide%20main.

[36] R.Dean Straw and Gerald L. Hall. Antenna Height and Communications Effectiveness: Second Edition – A Guide for City Planners and Amateur Radio Operators. Technical report, The American Radio Relay League, Inc., 1999. https://www.arrl.org/files/file/antplnr.pdf.

[37] DivideByZero (Divbyz). Flexible filament—thermoplastic polyurethane (tpu) for 3d printing. https://www.divbyz.com/knowledge-center/materials/tpu.

[38] Ravichandran Ranjith, Rho Shin Myong, and Sangwook Lee. Computational investigation of lightning strike effects on aircraft components. *International Journal of Aeronautical and Space Sciences*, 15(1):44–53, 2014. https://www.researchgate.net/publication/277577692_Computational_Investigation_of_Lightning_Strike_Effects_on_Aircraft_Components.

# Appendices

# Appendix 8.1

The bandwidth calculations were done using Excel sheet:

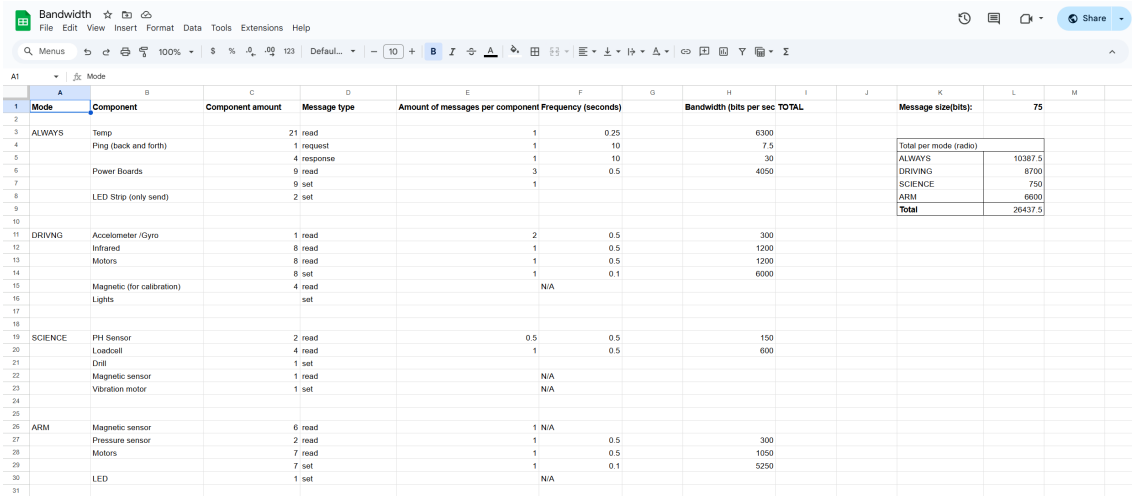

Bandwidth

| Mode | Component | Component amount | Message type | Amount of messages per component | Frequency (seconds) | Bandwidth (bits per sec | TOTAL | Message size(bits): | 75 |
|---|---|---|---|---|---|---|---|---|---|
| ALWAYS | Temp | 21 | read | 1 | 0.25 | 6300 | | | |
| | Ping (back and forth) | 1 | request | 1 | 10 | 7.5 | | Total per mode (radio) | |
| | | 4 | response | 1 | 10 | 30 | | ALWAYS | 10387.5 |
| | Power Boards | 9 | read | 3 | 0.5 | 4050 | | DRIVING | 8700 |
| | | 9 | set | 1 | | | | SCIENCE | 750 |
| | LED Strip (only send) | 2 | set | | | | | ARM | 6600 |
| | | | | | | | | **Total** | 26437.5 |
| DRIVNG | Accelometer /Gyro | 1 | read | 2 | 0.5 | 300 | | | |
| | Infrared | 8 | read | 1 | 0.5 | 1200 | | | |
| | Motors | 8 | read | 1 | 0.5 | 1200 | | | |
| | | 8 | set | 1 | 0.1 | 6000 | | | |
| | Magnetic (for calibration) | 4 | read | | N/A | | | | |
| | Lights | | set | | | | | | |
| SCIENCE | PH Sensor | 2 | read | 0.5 | 0.5 | 150 | | | |
| | Loadcell | 4 | read | 1 | 0.5 | 600 | | | |
| | Drill | 1 | set | | | | | | |
| | Magnetic sensor | 1 | read | | N/A | | | | |
| | Vibration motor | 1 | set | | N/A | | | | |
| ARM | Magnetic sensor | 6 | read | 1 | N/A | | | | |
| | Pressure sensor | 2 | read | 1 | 0.5 | 300 | | | |
| | Motors | 7 | read | 1 | 0.5 | 1050 | | | |
| | | 7 | set | 1 | 0.1 | 5250 | | | |
| | LED | 1 | set | | N/A | | | | |

*Figure 1: Channel Capacity calculations for the rover*

# Appendix 8.2

All the values of materials in the table were taken from Microwave Studio, besides TPU and CFRB, which were introduced as new materials in the BOM library

| Material | Type | $\mu$ | $\varepsilon$ | El. Cond.$[S/M]$ | Mag. Cond. $[1/Sm]$ | $\rho[kg/m^3]$ |
|---|---|---|---|---|---|---|
| TPU[37] | Normal | 1 | 3.60 | 10 | 0 | 1140 |
| Al | Lossy Metal | 1 | - | $3.56 \times 10^7$ | $\approx 0$ | 2700 |
| CFRB[38] | Normal | 1 | 3.20 | $7.94 \times 10^{-7}$ | 0 | 1600 |
| Sandy Soil(Dry) | Normal | 1 | 2.53 | 0 | 0 | 1550 |

*Table 1: BOM of the project*

# Appendix 8.3

The return-loss results of the 2.4 GHz antenna are recorded in *Table 3*.

Each component is:

- g is the ground diameter
- l is the length of the quarter monopole
- r is the radius of the quarter monopole

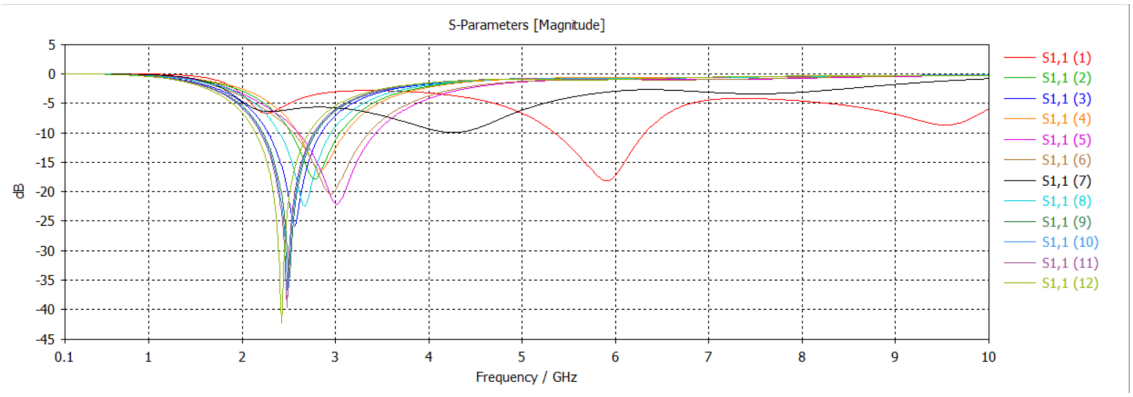


*Figure 2: Return loss S11 for the 2.4 GHz quarter monopole antenna*

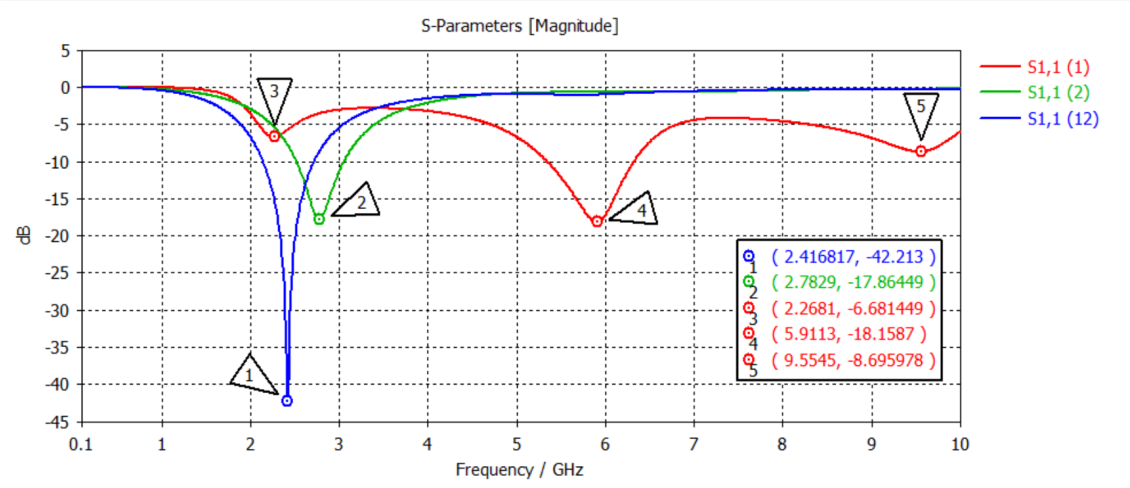


*Figure 3: Return loss S11 for 3 different points for the 2.4 GHz antenna*

| S11(i) | g[cm] | l[cm] | r[cm] |
|---|---|---|---|
| 1 | 6.25 | 2.75 | 0.15 |
| 2 | 6.25 | 2.75 | 0.63 |
| 3 | 6.25 | 3.13 | 0.63 |
| 4 | 6.25 | 2.65 | 0.63 |
| 5 | 6.25 | 2.75 | 0.50 |
| 6 | 6.25 | 2.85 | 0.30 |
| 7 | 6.25 | 2.85 | 0.30 |
| 8 | 6.75 | 2.85 | 0.63 |
| 9 | 6.75 | 3.15 | 0.63 |
| 10 | 6.75 | 3.18 | 0.63 |
| 11 | 6.75 | 3.20 | 0.63 |
| 12 | 6.75 | 3.30 | 0.63 |

*Table 2: Parametric trials of the 2.4GHz antenna*

# Appendix 8.4

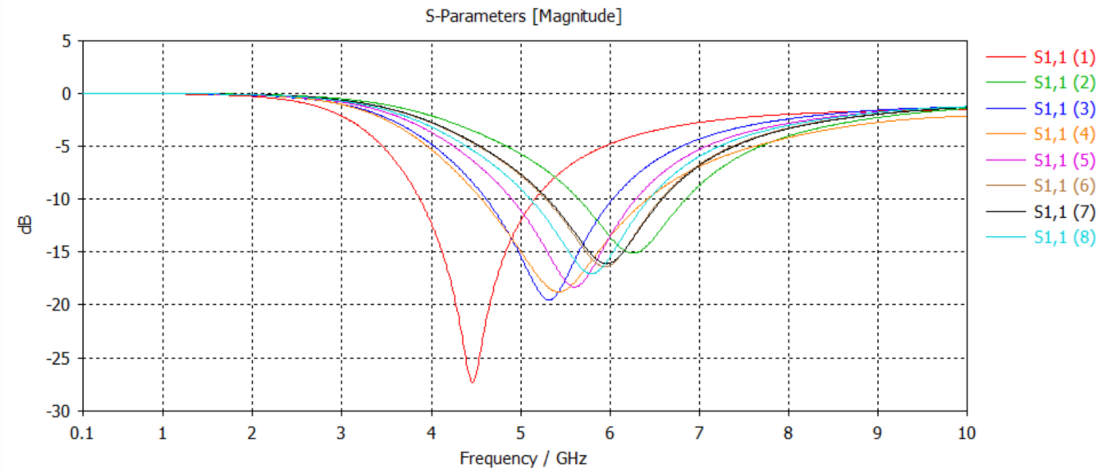


*Figure 4: Return loss S11 for the 5.8 GHz quarter monopole antenna*

| S11(i) | g[cm] | l[cm] | r[cm] |
|---|---|---|---|
| 1 | 4.00 | 1.74 | 0.26 |
| 2 | 2.59 | 1.29 | 0.26 |
| 3 | 2.59 | 1.59 | 0.26 |
| 4 | 2.59 | 1.59 | 0.26 |
| 5 | 2.59 | 1.49 | 0.26 |
| 6 | 2.59 | 1.39 | 0.26 |
| 7 | 2.54 | 1.39 | 0.26 |
| 8 | 2.59 | 1.44 | 0.26 |

*Table 3: Parametric trials of the 5.8GHz half-wavelength dipole*

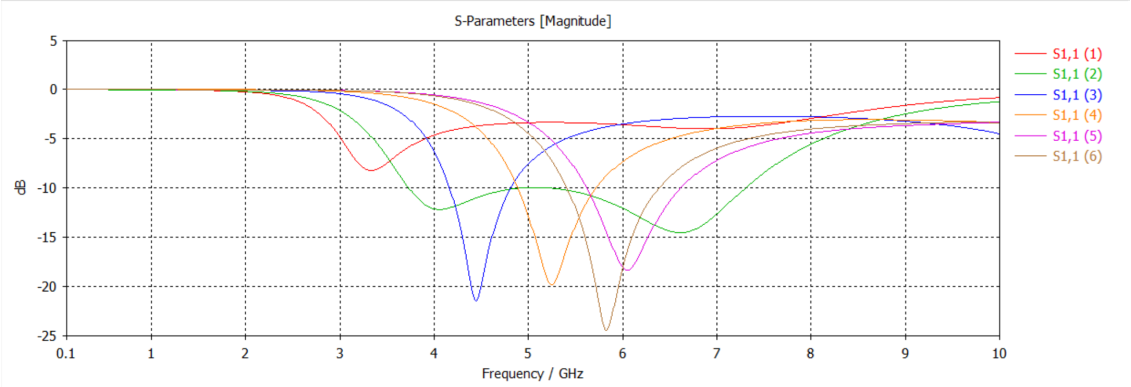


*Figure 5: Return loss S11 for the 5.8 GHz half-wavelength dipole antenna*

| S11(i) | h[cm] | l[cm] | r[cm] |
|---|---|---|---|
| 1 | 0.20 | 1.92 | 0.10 |
| 2 | 0.10 | 1.90 | 0.10 |
| 3 | 0.10 | 2.19 | 0.10 |
| 4 | 0.10 | 2.59 | 0.10 |
| 5 | 0.10 | 2.59 | 0.26 |
| 6 | 0.10 | 2.59 | 0.26 |

*Table 4: Parametric trials of the 5.8GHz half-wavelength dipole*

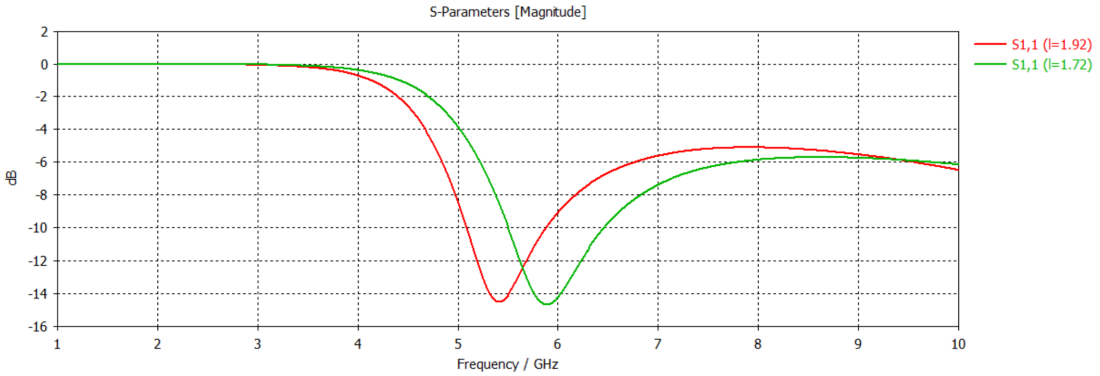


*Figure 6: Return loss S11 for the 5.8 GHz plane reflector feed*

| S11(i) | h[cm] | l[cm] | r[cm] |
|---|---|---|---|
| 1 | 0.10 | 1.92 | 0.10 |
| 2 | 0.10 | 1.72 | 0.10 |

*Table 5: Parametric trials of the 5.8GHz antenna*